

Final Report

Contract Number N00014-88-J-1100

(Handwritten signature)

AD-A267 292



PROCESSING AND PROTECTION OF
HIGH TEMPERATURE STRUCTURAL
MATERIALS

S DTIC
ELECTE
AUG 02 1993 **D**
A

Submitted by
Ellis D. Verink, Jr.
Principal Investigator

CENTER FOR APPLIED THERMODYNAMICS AND CORROSION

Panel on Environmental Stability of High Temperature
Materials For Advanced Technological Applications

This document has been approved
for public release and sale; its
distribution is unlimited.

Department of Materials Science and Engineering
University of Florida
Gainesville, Florida, 32611

~~93-5-00-06-3~~

93-11942



90pgs.

FINAL REPORT

PROCESSING AND PROTECTION OF HIGH TEMPERATURE STRUCTURAL MATERIALS

Contract Number: N00014-88-J1100

Executive Summary

A. Description of Scientific Research Goals

Our objective was to develop a greatly improved understanding of the thermodynamic basis for processing and performance enhancement of Nb and Ta based alloys in order to provide better, scientifically-based support for current engineering efforts aimed at development of high temperature structural aerospace applications.

B. Significant Results

A number of significant accomplishments have been made by the cooperating teams of researchers involved in this program. At the University of Florida, DeHoff and Brady have completed final modification of a computer program for calculating thermochemical diagrams of the type calculated by Dr. Pourbaix for high temperature oxidation. The development of such a program was one of the major milestones of the project. The program is ready for distribution upon request.

Dr. R.T. DeHoff's team has developed, a computer program which is designed to establish the connection between experimentally observable information about diffusion in multicomponent systems (i.e., composition profiles and Kirkendall shifts) and the jump frequencies of the components. This new formulation makes the case of quaternary diffusion tractable for the first time (spin-off from diffusion milestone).

Dr. Ebrahimi's team have investigated diffusion behavior of aluminum in niobium and niobium alloys. The intrinsic diffusion coefficient for aluminum in niobium has been determined for binary alloys containing 1.5 to 3.0 atomic percent aluminum. Typical values for the 3.0 atomic percent alloy range from 0.213×10^{-11} to 3.827×10^{-11} cm²/sec over a temperature range of 1325-1525°C, with an average temperature dependence of 78.8 K cal/mol. (program milestone). Apparently diffusion rates in couples based on the ternary Nb-Ti-Al system are significantly faster than in binary couples. There is evidence that Al and Ti co-diffuse. (spin-off from diffusion studies).

Thermogravimetric kinetic studies (in this program and elsewhere) have shown that alloys of the X-Ti-Al₂ type (where X = Nb or Ta) are among the most promising alloys found so far, from the standpoint of their ability to withstand high temperature oxidation conditions. Nonetheless, while the corrosion kinetics are reduced when compared with alloys having less than 40 atomic percent Al, the oxidation rates still are linear, indicating that attack has not ceased. It appears that surface modification strategies will need to be invoked in order to provide more complete protection from high temperature oxidation for this class of alloys. Using ion implantation of Y, Ce and Al has not proved promising in enhancing

oxidation behavior of ternary Nb-Ti-Al alloys.

Contradictory conclusions about the role of nitrogen as reported in the oxidation literature by various authors, suggest that nitrogen may be an important factor contributing to the wide scatter in kinetic data reported. Because the structures of interest to this program will operate in the presence of nitrogen, it is considered vital that the role of nitrogen be established eventually.

Basic science activities at NIST have included the determining of more accurate data for the heat of formation of NbO_2 , as well as the completing of computer optimization of the Nb-Al binary system. This information could be used, when (and if) completed, in conjunction with time-dependent and composition-dependent data developed at U of F to estimate diffusion rates in Nb-Al intermetallics.

"Hand calculated" thermochemical diagrams have been drawn by Pourbaix for Al-O, Ti-O, Nb-O, Si-O and the C-O systems (a program milestone). The computerization of the calculation and plotting of thermochemical diagrams of the type developed by Pourbaix has been completed (program milestone).

Accession For	
NTIS CRA&I	<input checked="checked" type="checkbox"/>
DTIC TAB	<input type="checkbox"/>
Unannounced	<input type="checkbox"/>
Justification	
By <i>per lti</i>	
Distribution /	
Availability Codes	
Dist	Avail and/or Special
A-1	

DTIC QUALITY INSPECTED 3

TECHNICAL REPORT

This Final Report covers the time period from March 1991 to March 1993 during which time research was conducted under a no-cost extension.

High Temperature Oxidation Behavior of Candidate Alloys

The team working under the direction of Dr. Ellis D. Verink, Jr. has continued the studies aimed at elucidating the oxidation mechanisms for Nb-Ti-Al alloys exposed to air and oxygen at elevated temperatures.

Two additional publications have been completed covering various aspects of research. The titles and Abstracts of these publications are included in this section of the report. Copies of the full manuscripts are attached to this report.

Brady, M.P., Hanrahan, R.J., and Verink, E.D., "The Role of the σ , γ , and β Phases During the Oxidation of Nb-Ti-Al Alloys". To be presented at the TMS Fall Meeting, October 17-21, 1993, Pittsburgh, Pa.

ABSTRACT

Based on the results of this study, efforts to develop oxidation resistant Nb-Ti-Al alloys should focus on single phase γ alloys, or alloys which consist predominantly of the γ phase. If multiphase structures are necessary, processing routes which modify the distribution of phases in the microstructure (e.g., spacing between σ and γ phases) appears potentially promising.

For Nb-Ti-Al alloys exposed in air at 1200° and 1400°C: 1) The transformation from a β decomposed structure to $\sigma + \gamma$ is sufficiently rapid that oxidation behavior seems unaffected. 2) The γ phase is the source of α -Al₂O₃ and the σ phase is the source of AlNbO₄ in oxide scales formed by $\sigma + \gamma$ alloys. In Nb-Ti-Al alloys, both σ and γ phases oxidize to form TiO₂. 3) Oxidation behavior is influenced by σ/γ interfacial area, σ/γ volume fraction and the continuity of the individual phases. Factors which increase the influence of γ phase improve oxidation resistance. 4) The transition to protective alumina formation at high temperature is associated with the γ phase (not the β phase)

Hanrahan, R.J., Brady, M.P., Verink, E.D. and Withrow, S.P., "Effect of Yttrium Implantation on the Oxidation Behavior of Nb25-Ti25-Al50 at 1300 C and 1500 C, For presentation at the Fall Meeting of TMS, October 17-21, 1993, Pittsburgh, Pa.

ABSTRACT

The effect of ion-implanted yttrium on the oxidation behavior of Nb25-Ti25-Al50 was studied. Rectangular samples were implanted on two sides with 3×10^{15} ions/cm². Oxidation kinetics in air were studied using continuous thermogravimetric analysis. Exposures were conducted at 1300° and 1500°C for times ranging from 15 minutes to 144 hours. After

exposure, samples were examined by X-ray diffraction, scanning electron microscopy, electron microprobe analysis and Auger electron spectroscopy. No significant improvement in the implanted samples versus non-implanted samples was detected using any of these techniques. The lack of reactive element effect (i.e., slower oxidation kinetics, or improved scale adherence) in this alloy is attributed to a rapid initial transient oxidation period during which the implanted region is consumed by the advancing oxidation front.

Modelling Diffusion Behavior in Multicomponent Systems

Dr. R.T. DeHoff's team has developed, a computer program which is designed to establish the connection between experimentally observable information about diffusion in multicomponent systems (i.e., composition profiles and Kirkendall shifts) and the jump frequencies of the components. The traditional description of interdiffusion is based on Fick's Laws, and involves tedious experimental methods (involving numerous diffusion couples) and mathematical manipulation to obtain the 2×2 matrix of interdiffusion coefficients for a ternary system. The values of D_{ij} , which can be evaluated only at points of intersection of the composition paths of the diffusion couples involved, unfortunately, are only indirectly related to the actual motions of atoms of the three components through the lattice. Thus it is not possible to link the measured diffusion coefficients with physical attributes such as size, electronegativity, group number, etc., using the traditional methods.

For a system having four or more components (e.g., Nb-Al-Ti-O) the 3×3 matrix of interdiffusion coefficients cannot be evaluated from experimental information since the quaternary case would require intersection of composition paths from three diffusion couples, an event that has negligible probability.

DeHoff's alternate formulation makes the quaternary case tractable. He began with an approximate concept which he calls the "penetration tendency approach". The computer program under development is a more rigorous treatment starting from this viewpoint. Program input is information about the composition dependence of the jump frequencies for each component. For any diffusion couple, this information is used to compute the flux and composition profiles for each component. The imbalance of atom fluxes gives the vacancy flux at each position, and from this information the Kirkendall shift can be computed. With the help of the computer, it is not difficult to compute a pattern of composition paths and Kirkendall shifts from a given input pattern of jump frequencies. Comparison of the calculated patterns with experimental measurements permits assessment of the assumed jump frequency functions, and points the direction to modifications that will lead to better agreement with experimental data. As recently reported, this program now is operating for the case of an arbitrary number of components flowing through an isomorphous diffusion couple. An attempt to model the experimental results for the Fe-Ni-Co system shows that the comparison of the experimental composition path pattern agreed with the computed path pattern within a few atomic percent. Future plans involve trying the program on well explored data from the Cu-Ag-Au system, and the Cu-Ni-Zn system. These are important steps toward our goal of being able to predict composition path patterns and Kirkendall shifts which evolve during diffusion controlled oxidation of multicomponent alloys.

Diffusion Studies in the Nb-Al and the Nb-Ti-Al Systems

Diffusion studies have been conducted under the direction of Dr. F. Ebrahimi. Mr. J.G. Luiz-Aparicio completed a Masters Thesis entitled, "A Study of Diffusivity in the BCC Solid Solution of the Nb-Al and Nb-Ti-Al System". The Abstract of this thesis is included in this report, and a full copy of the thesis is appended.

ABSTRACT

Niobium alloys with improved resistance to oxidation are needed for use as structural alloys. The feasibility of forming protective alumina scales in Nb-Al-X alloys by the selective oxidation of aluminum has been demonstrated and also has been shown that a low aluminum diffusivity is the major factor limiting the selective oxidation of aluminum. Additions of certain elements such as titanium are thought to have a beneficial action on accelerating this diffusivity but information on the effect of alloying additions is limited.

In this thesis, diffusion studies in the binary Nb-Al system by the Matano-Boltzmann method, and diffusion analyses in the ternary Nb-Al-Ti system through concepts such as Kirkendall shift, crossover displacements, penetration tendencies and composition paths, were conducted to evaluate the diffusivity of Al and the effect of Ti on Nb-based alloys.

Nb-Al, Nb-Ti, Nb-Al-Ti (b.c.c.) solid solutions were prepared by arc-melting and were homogenized in a high vacuum furnace before the fabrication of diffusion couples. Bonding of the diffusion couples was obtained by hot pressing in a temperature range of 700°-1000° C for two hours. A fine dispersion of yttria chopped fibers was used as markers. The diffusion treatment temperatures were varied from 1350°-1550° C and 1200°-1400° C for the binary and ternary studies respectively. Microprobe analysis was employed for the evaluation of composition profiles in all the diffusion couples.

The interdiffusion coefficient for the b solid solution of Nb-Al system varied linearly with Al concentration in the range of 1-3 at% and it followed a linear Arrhenius behavior as a function of temperature in the range of 1350°-1550° C. The average activation energy for diffusivity of Al in Nb was calculated to be 78.4 Kcal/mole with a frequency factor of $4.5 \times 10^{-2} \text{ cm}^2/\text{sec}$. These values are smaller than those reported in the literature for a higher temperature range. This discrepancy is attributed to the differences in the evaluation method and the temperature range. The influence of the di-vacancy mechanism, which is known to operate at higher temperatures in Nb, may account for the higher diffusion rate and activation energy.

The composition path and penetration tendencies in the Nb-Ti-Al system suggest that Ti is the fastest element in the b solid solution. Qualitatively the penetration tendencies correlate with the melting point of the alloys. The results of Kirkendall shift measurement were found to be in agreement with the calculated crossover displacement. The results obtained in this study suggest that the addition of Ti to the binary alloy increases the general diffusivity of the system.

A paper entitled "Fracture Toughness of Sigma plus "X" Microstructures in the Nb-Ti-Al System has been submitted to the Journal of Materials Science and Engineering. Authors are F. Ebrahimi, D.T. Hoelzer and J.R. Castillo-Gomez. The full paper is attached, however the Abstract is included here.

ABSTRACT

The Nb-Ti-Al system offers many intermetallics that potentially can be used for high temperature structural applications. The objective of this study has been to improve room temperature toughness of the sigma phase ($\text{Nb}_2\text{Al}+\text{Ti}$), which has a high melting point and good high temperature strength, with inclusion of semi-ductile phases. The incorporation of second-phase particles has been found to enhance the toughness of the sigma phase considerably. Fractographic analysis has revealed that when the interface between the particles and the matrix is strong, the second phase particles impede the crack front by trapping the crack tip due to plasticity. The crack propagation continues by a reinitiation process ahead of the crack tip. Consequently, the crack is bridged by the second-phase particles. The cleavage of the second-phase particles results in the final separation of the crack faces. In the weakly-bound particles, the level of internal stresses has been found to influence the crack path, and therefore, the toughness. In this paper the effects of the volume fraction, size and distribution of the particles, as well as their nature on the fracture path and toughness are discussed.

No activities were undertaken during this period by either NIST or CEBELCOR. Results of their research activities appear in earlier reports.

THE ROLE OF THE σ , γ , AND β PHASES DURING THE OXIDATION OF Nb-Ti-Al ALLOYS

M.P. Brady, R.J. Hanrahan, Jr., E.D. Verink, Jr.

INTRODUCTION

An extensive investigation of the factors affecting the selective oxidation of aluminum from niobium to form protective alumina scales was conducted by Perkins and Meier et al. from 1986-1989 [1]. A major result of this study was the identification of the Nb-Ti-Al system as a potential base for oxidation resistant high temperature alloys. The most promising alloys in terms of high temperature oxidation resistance were located in the aluminum-rich side of the central portion of the phase diagram.

Alloy microstructure was identified as playing a key role in the development of oxidation resistance in the Nb-Ti-Al system. Oxidation was observed to follow a general pattern of protective alumina formation at high temperature and rapid parabolic oxidation at intermediate temperature [1a]. Study of Nb-Ti-Al alloys modified with small amounts of Cr and V suggested that the transition to protective alumina formation at high temperature was related to a change in microstructure from a two-phase σ ($\text{Nb}_2\text{Al}+\text{Ti}$) + γ ($\text{TiAl}+\text{Nb}$) microstructure to a single phase β (high temperature BCC solid solution phase) microstructure [1b].

Lack of phase equilibria information for the Nb-Ti-Al system limited much of the design and interpretation of the Perkins + Meier study to an empirical approach based on systematically varying alloy composition and interpreting results in terms of alloy compositional variables. However, phase equilibria in the Nb-Ti-Al system has been the subject of much recent experimental and computational study (including the efforts of Hoelzer and Ebrahimi described in this report) [2,3,4]. While still incomplete, this new information provides a basis for the systematic study of the role of **microstructure** during the oxidation of Nb-Ti-Al alloys. Such information is necessary in order to develop a mechanistic understanding of oxidation in the Nb-Ti-Al system and ultimately to optimize oxidation resistance. This section of the report presents an overview of efforts to define the roles of the σ , γ , and β phases during oxidation at both intermediate and high temperature. Further details are available in reference 5.

EXPERIMENTAL

Oxidation was studied at 1200°C and 1400°C in air. The test temperatures were chosen to study the two regimes of oxidation behavior in this system: nonprotective oxidation kinetics at intermediate temperatures (1200°C) and protective oxidation kinetics at high temperatures (1400°C). All oxidation experiments were conducted in air because most "real-world" applications involve exposure in air.

1200°C

At 1200°C in air, a complex oxide scale consisting of TiO_2 , AlNbO_4 , and noncontinuous $\alpha\text{-Al}_2\text{O}_3$ is formed by $\sigma+\gamma$ alloys. The scale is not protective and rapid linear oxidation kinetics are observed. Two alloy microstructural variables were isolated in order to elucidate the role of the σ and γ phases during oxidation: the σ/γ interfacial area and the σ/γ volume fraction. Alloy compositions and microstructures are listed in Table 1.

σ/γ Interfacial Area

Most alloys which fall within the $\sigma+\gamma$ two phase field at 1200°C solidify from the β phase (refer to the liquidus projection shown in Figure 1 and the 1200°C isotherm shown in Figure 2). However, the β phase in this composition range is not stable and decomposes during cooling to a complex, multiphase microstructure which depends on the rate of cooling. On exposure at 1200°C, the β decomposed microstructure transforms to a $\sigma+\gamma$ microstructure.

The $\sigma+\gamma$ microstructure which is formed on exposure at 1200°C is sensitive to the pre-exposure β decomposed microstructure. By changing the solidification conditions and therefore the β decomposed microstructure, different σ/γ interfacial areas can be produced without changing the volume fraction or composition of the $\sigma+\gamma$ microstructure. Alloy #3 was selected for study because it contained almost equal volume fractions of the σ and γ phases at 1200°C (refer Table 1 and Figures 1 and 2) and because detailed information on the as-cast and 1200°C microstructures was available [4].

Three types of oxidation test samples were prepared from alloy #3:

- 1) As-received arc-melted
- 2) Electromagnetic Levitation (EML)
- 3) Arc-melted/aged

The EML oxidation test samples were cut from the arc-melted button, remelted by induction in an electromagnetic levitation (EML) apparatus, and dropped onto a copper chill plate. Processing by EML creates much faster solidification and cooling rates than bulk arc-melting and produces a β decomposed microstructure which transforms to a finer $\sigma+\gamma$ microstructure on exposure at 1200°C than the β decomposed microstructure produced by arc-melting. The arc-melted/aged oxidation test samples were cut from the arc-melted button and aged for 4 hours at 1200°C (furnace cooled) in order to produce a $\sigma+\gamma$ microstructure. Comparison of the oxidation behavior of the arc-melted/aged oxidation test samples with the arc-melted test samples was used to determine if the $\sigma+\gamma$ transformation reaction itself affected oxidation behavior.

σ/γ Volume Fraction

Five alloys from the same 1200°C tie-line were selected for study: single phase γ (#1), predominantly γ (#2), equal volume fraction (v/o) of σ and γ (#3), predominantly σ (#4), and single phase σ (#5). The alloy compositions are listed in Table 1 and plotted on the 1200°C isotherm shown in Figure 2. By selecting the alloys from the same 1200°C tie line, the compositions of the σ and γ phases were held constant. This allowed for a direct

comparison of the σ/γ volume fraction with oxidation behavior. All oxidation test samples were prepared from as-received arc-melted material.

1400°C

At 1400°C in air, Perkins + Meier et al. demonstrated that Nb-Ti-Al alloys which contain greater than 44 atom percent (a/o) aluminum at a niobium to titanium ratio of approximately one to one form a protective alumina scale [1a]. The alumina scale forms as a continuous layer at the metal/scale interface and cuts off the growth of a rapidly forming transient oxidation product—a complex mixture of aluminum and titanium niobates. Small additions of chromium and vanadium reduce the minimum aluminum content necessary for protective alumina formation to 37 a/o [1b].

The Nb-Ti-Al-Cr-V alloys were single phase β at high temperatures, and formed a protective alumina scale. At lower temperatures, the Nb-Ti-Al-Cr-V alloys were two-phase $\sigma+\gamma$, and did not form a protective alumina scale. The transition to protective alumina formation was attributed to the transformation of the microstructure from $\sigma+\gamma$ to β . It was speculated that aluminum diffusion is significantly increased because the crystal structure of the β phase is body centered cubic (BCC) [1b]. The crystal structure of the σ and γ phases is tetragonal. An increase in the rate of aluminum diffusion would favor the formation of a continuous $\alpha\text{-Al}_2\text{O}_3$ layer.

Little information is available as to the effects of chromium and vanadium on the phase equilibria of Nb-Ti-Al alloys. However, recent studies of phase equilibria in the Nb-Ti-Al system place the alloys without chromium and vanadium additions which form protective alumina scales in the γ phase field and not the β phase field at 1400°C (Figure 3) [2,3]. From both a mechanistic and alloy development point of view, it is very important to determine if the transformation to protective alumina formation results from an increase in the rate of aluminum diffusion because of a microstructural transformation to the β phase or if some other mechanism is responsible.

Two Nb-Ti-Al alloys were selected for study at 1400°C. The first alloy (#6) contained more aluminum than the minimum 44 a/o needed to form a protective continuous alumina layer. The second alloy (#3) contained less aluminum than the 44 a/o necessary for protective alumina formation. The alloy compositions are listed in Table 2 and plotted on the calculated 1400°C isotherm shown in Figure 3.

Test Sample Preparation

Arc-melted buttons (200 g) were supplied by United Technologies (Pratt and Whitney). Cross-sectional microprobe analysis indicated that macro-segregation was not present [4]. Alloys #1, #2, #4, #5, and #6 were studied only in the as-received arc-melted condition. Three types of alloy #3 test samples were studied: as-received arc-melted, arc-melted/aged, and EML. Test samples (approximately 1 cm x 1 cm x 1 mm) were sectioned from the bulk processed material using a low speed diamond saw and polished to a 50 micron finish by standard metallographic techniques. Surface microcracks were present in the alloy #4 and alloy #5 test samples after polishing. These alloys contained the

largest quantities of the σ phase, which is extremely brittle. The oxidation behavior of alloy #4 and alloy #5 is not believed to have been significantly affected by the presence of the surface microcracks because the oxidation kinetics data were reproducible. However, all oxidation kinetics data concerning alloy #4 and alloy #5 should be viewed with caution.

Oxidation

To begin an oxidation experiment, the test samples were lowered into the reaction chamber hot zone at temperature. The test samples were removed from the hot zone and air cooled to room temperature at the conclusion of each experiment. Oxidation kinetics were monitored continuously by thermogravimetry (TGA) at nominal temperatures of 1200°C (alloys #1-#5) and 1400°C (alloys #3 and #6) for exposure times up to 48 hours in air using a CAHN 2000 Microbalance and a CAHN RG Microbalance. The actual testing temperature was nominally $\pm 10^\circ\text{C}$ of the test temperature.

The temperature of the furnace/TGA apparatus used to study the effect of varying the σ/γ volume fraction was $1200^\circ\text{C} \pm 10^\circ\text{C}$. However, the temperature of the furnace/TGA apparatus used to study the effect of varying the σ/γ interfacial area was $1218^\circ\text{C} \pm 10^\circ\text{C}$. Therefore, two sets of as-received arc-melted alloy #3 test samples were exposed: the first for comparison with the σ/γ volume fraction alloys and the second for comparison with the σ/γ interfacial area EML and arc-melted/aged test samples. No significant differences in oxidation behavior were observed between the alloy #3 test samples exposed at 1218°C and 1200°C ; although rate of oxidation was slightly higher at 1218°C . For simplicity, only the nominal temperature of 1200°C is quoted in the remainder of the text.

The test samples were characterized by x-ray diffraction, optical microscopy, scanning electron microscopy (SEM), microprobe (wavelength dispersive analysis mode), Transmission Electron Microscopy (TEM), and in-situ high temperature x-ray diffraction. Stereological measurements were made on SEM backscatter images using a Quantimet 5000 Image Analysis System.

RESULTS AND DISCUSSION

$\sigma+\gamma$ Interfacial Area (1200°C)

Alloy Microstructure

The microstructure of the 200 g alloy #3 arc-melted button was coarse and extremely complex (Figure 4). TEM analysis was attempted only on smaller re-arc-melted samples of alloy #3 in which the microstructure was not as coarse [4]. Based on comparison with re-arc-melted samples, the microstructure of the bulk 200 g arc-melted button of alloy #3 consisted of retained β_2 (ordered β), the orthorhombic phase, the γ phase, and an ω -type phase.

The microstructure of the EML test samples was of a much finer scale than the microstructure of the bulk arc-melted test samples (Figure 5). TEM analysis indicated that a β_2 matrix was retained at room temperature [4]. Only the orthorhombic phase was present as a matrix precipitate [4]. The microstructures of the arc-melted and EML test samples are consistent with solidification from the β phase field and are therefore in agreement with the liquidus projection (Figure 1).

Aging arc-melted alloy #3 for four hours at 1200°C (furnace cool) resulted in a complete transformation to a $\sigma + \gamma$ microstructure (Figure 6) [4]. The microstructure consisted of (approximately) 55 volume percent (v/o) σ and 45 v/o γ . The presence of σ and γ in the observed proportions is consistent with the 1200°C isotherm (Figure 2).

After one hour of exposure at 1200°C, the β decomposed microstructures of the arc-melted and EML test samples were fully transformed to $\sigma + \gamma$. The microstructure of the arc-melted/aged test sample remained $\sigma + \gamma$. The σ/γ volume fractions, 55 v/o σ and 45 v/o γ , were the same (within measurement error) for all three sample types and all exposure times.

The σ/γ interfacial area, as measured by the surface-area-per-unit-volume of the γ phase, decreased for all three sample types between 1 and 12 hours of exposure at 1200°C (Figure 7). The decrease in the σ/γ interfacial area at constant σ/γ volume fraction indicates that the $\sigma + \gamma$ microstructures coarsen during the first 12 hours of exposure. From 12 hours to 48 hours of exposure, the σ/γ interfacial areas did not vary with exposure time.

The σ/γ interfacial areas of the arc-melted and arc-melted/aged test samples were essentially identical beyond 12 hours of exposure. However, the σ/γ interfacial area of the EML test sample was greater than the arc-melted and arc-melted/aged samples for all exposure times studied. Therefore, the EML test samples transformed to a finer $\sigma + \gamma$ microstructure than the arc-melted test samples.

Oxidation Kinetics

The TGA curves for the arc-melted, EML, and arc-melted/aged alloy #3 test samples show that parabolic oxidation kinetics were followed for all three sample types at 1200°C in air (Figure 8). The oxidation kinetics of the arc-melted and arc-melted/aged test samples were similar. However, a moderate decrease in the rate of oxidation was observed for the EML test samples.

The microstructures and the oxidation kinetics observed for the arc-melted and arc-melted/aged test samples were similar. Therefore, the $\sigma + \gamma$ transformation reaction itself did not significantly affect oxidation behavior at 1200°C. This supposition is supported by TEM phase equilibria studies which demonstrated that the transformation to a $\sigma + \gamma$ microstructure was extremely rapid and occurred within the first two minutes of exposure at 1200°C [6]. A rapid transformation minimizes the time available for oxidation behavior to be affected.

The linear rate of oxidation was inversely proportional to the σ/γ interfacial area. The ratio of the linear rates of oxidation calculated from the TGA curves between 24 and 48 hours

for the arc-melted and EML test samples was 1.39. The corresponding ratio of the σ/γ interfacial areas of the arc-melted and EML test samples is 1.46^{-1} . The similarity of these ratios is consistent with a direct relationship between the σ/γ interfacial area and the linear rate of oxidation.

Oxide Scale Microstructure

X-ray diffraction analysis of the oxidation products indicated that the oxide scales formed by all three sample types consisted primarily of TiO_2 , AlNbO_4 , and $\alpha\text{-Al}_2\text{O}_3$. Rutile TiO_2 was the predominant oxidation product for all three sample types and for all exposure times. No differences in the oxidation products formed by the arc-melted and arc-melted aged test samples were detected. However, $\alpha\text{-Al}_2\text{O}_3$ was present in the greatest amount in the oxide scale formed by EML test sample after 3 hours of exposure. It was not possible to determine if this trend continued for the longer exposure times because the complexity of the diffraction patterns limited the analysis to a qualitative determination of the relative amounts of the oxides present. Broad and overlapping diffraction peaks are characteristic of the oxides formed by niobium-based alloys and complicate interpretation of diffraction patterns [1c,7]. A number of small unidentified peaks were also present.

The microstructural features of the oxide scale were classified into three regions (Figure 9):

- 1) unoxidized base alloy ($\sigma+\gamma$)
- 2) selective oxidation zone ($\alpha\text{-Al}_2\text{O}_3$ particles in a layer of unoxidized σ)
- 3) outer oxide scale (complex mixture of TiO_2 , AlNbO_4 , and discrete bands of $\alpha\text{-Al}_2\text{O}_3$ particles)

The selective oxidation zone was observed in all three test sample types. After a transient growth period, which occurred within one hour of exposure of the arc-melted/aged test samples and between 3 and 12 hours of exposure of the arc-melted and EML test samples, the selective oxidation reached a steady-state thickness. The final thickness of the selective oxidation zone was approximately the same for test samples produced by all three processing treatments.

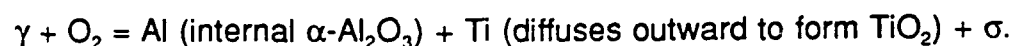
Microprobe measurements show that titanium was depleted and niobium and aluminum were enriched directly underneath the selective oxidation zone in both the σ and γ phases (Figure 10). When the microprobe data are plotted on the 1200°C phase diagram, it becomes apparent that the compositions of both the σ phase and the γ phase moved away from the titanium-rich corner of the phase diagram along the σ and γ phase boundaries (Figure 11). This result suggests that titanium diffuses faster than niobium and aluminum at 1200°C .

The enrichment of aluminum and niobium in the σ and γ phases underneath the oxide scale is a consequence of the shape of the σ and γ phase boundaries, which move away from the titanium-rich corner of the phase diagram at close to a 1:1 niobium to aluminum ratio. Because the composition path of the individual phases falls so closely to the phase boundaries, it is believed that local equilibrium was approached. (A slight deviation of the

γ phase composition path from the γ phase boundary was observed. It may be the result of oxygen content in the alloy which would be expected to shift the phase boundary, or perhaps slight differences in temperature between the experiments used to determine the phase boundary and the oxidation experiments of this study).

Proposed Oxidation Sequence for Alloy #3 at 1200°C in Air

At the start of oxidation, titanium diffuses rapidly outward from both the σ phase and the γ phase to form TiO_2 . Concurrently, the aluminum rich γ phase is selectively oxidized to form $\alpha\text{-Al}_2\text{O}_3$. The σ phase is initially protected because the aluminum rich γ phase acts as an oxygen getter. The loss of aluminum and titanium from the γ phase results in a transformation to the σ phase according to:



This process forms a layer of unoxidized σ containing discrete $\alpha\text{-Al}_2\text{O}_3$ particles (the selective oxidation zone). As oxidation proceeds, the discrete $\alpha\text{-Al}_2\text{O}_3$ particles which are formed from selective attack of the γ phase become incorporated into the outer oxide scale as the σ phase which surrounds the $\alpha\text{-Al}_2\text{O}_3$ particles is oxidized to form AlNbO_4 and TiO_2 . The incorporation of $\alpha\text{-Al}_2\text{O}_3$ particles in the outer scale region indicates that oxidation proceeds mainly by inward oxygen transport. Because the outer oxide scale is not protective, oxygen continues to penetrate into the alloy. A new oxygen gradient is established and the selective oxidation zone is extended by continued selective attack of the γ phase (Figure 12). This oxidation sequence is similar to that observed by Rapp and Goldberg for Nb-Zr and Nb-Zr-Re alloys [7].

The selective oxidation zone achieves a steady-state thickness, which indicates that a balance is established between the rate of outer scale formation and the rate of advance of the selective oxidation zone. The linear rate of oxidation of alloy #3 was shown to be inversely proportional to the σ/γ interfacial area. This result implies that the σ/γ interface is involved in the rate controlling step. It is speculated that oxygen transport into the alloy may occur predominantly along the σ/γ interface or that oxygen adsorption takes place at the σ/γ interface.

The test samples produced by EML transformed to a finer $\sigma+\gamma$ microstructure (increased $\sigma+\gamma$ interfacial area) and exhibited a lower rate of oxidation than the test samples produced by arc-melting. The increased σ/γ interfacial area increased the extent to which oxygen is getterred by the aluminum-rich γ phase to form $\alpha\text{-Al}_2\text{O}_3$, which lowered the rate of oxidation.

σ/γ Volume Fraction (1200°C)

Alloy Microstructure

The five alloys selected for study were: single phase γ (#1), predominantly γ (#2), equal volume fraction of σ and γ (#3), predominantly σ (#4), and single phase σ (#5). The predicted and actual microstructures of alloys #1-#5 are listed in Table 1. Alloys #2, #3, and #4 consisted of a two phase $\sigma+\gamma$ microstructure after exposure at 1200°C. The γ

phase was continuous in alloy #2 and the σ phase was continuous in alloy #3 and alloy #4. The relative volume fractions of the σ and γ phases agreed reasonably well with the volume fractions predicted by the 1200°C isotherm (Figure 2). Please note that for this study, a phase was described as continuous if it appeared connected in cross-section and was present as greater than 50 volume percent.

Alloy #5 was single phase σ after exposure at 1200°C. However, alloy #1 was not single phase γ after exposure at 1200°C (Figure 2). A second phase, identified by x-ray diffraction as α_2 ($\text{Ti}_3\text{Al+Nb}$), was present as a minor phase in alloy #1. According to the liquidus projection (Figure 1), alloy #1 falls at the border of the β and α phase fields. The as-received arc-melted microstructure of alloy #1 was characteristic of solidification from the α phase field. It was not determined if α_2 was in equilibrium with the γ phase at 1200°C in alloy #1, which would suggest that the 1200°C isotherm is in error, or if α_2 was present as a solidification remnant. The presence of α_2 in the microstructure of alloy #1 after 48 hours of exposure at 1200°C suggests that the 1200°C isotherm may be in error. Further work is necessary to clarify this matter. However, of importance for this study is that alloy #1 contained the largest γ volume fraction of alloys #1-#5 and that the γ phase was continuous.

Oxidation Kinetics

The TGA curves of alloys #1-#5 show that the alloys rank in order of oxidation resistance by the volume fraction of the γ phase in the microstructure (Figure 13). Further, parabolic oxidation kinetics were observed when the σ phase was the continuous matrix phase and parabolic (approximate) oxidation kinetics were observed when the γ phase was the matrix phase. The rate of oxidation for all of the alloys was too high to be considered protective.

Oxide Scale Microstructure

The oxide scales formed by alloys #1-#5 consisted primarily of TiO_2 , AlNbO_4 , and $\alpha\text{-Al}_2\text{O}_3$. The x-ray diffraction patterns were extremely complex and limited the analysis to a qualitative determination of the relative amounts of the oxides present. A number of small unidentified peaks were also present.

Qualitatively, the amount of $\alpha\text{-Al}_2\text{O}_3$ formed by the alloys was related to the volume fraction of the γ phase in the microstructure and the amount of AlNbO_4 formed by the alloys was related to the volume fraction of the σ phase in the microstructure. The oxide scale formed by alloy #5 (single phase σ) contained the greatest amount of AlNbO_4 , but only trace amounts of $\alpha\text{-Al}_2\text{O}_3$. The oxide scale formed by alloy #1 (γ + small α_2) contained the greatest amount of $\alpha\text{-Al}_2\text{O}_3$. The diffraction pattern of the oxide scale formed by alloy #1 also contained a large number of unidentified peaks. Rutile TiO_2 was a major oxidation product in the scales formed by all five alloys.

Cross-section micrographs of alloys #1-#5 exposed for 48 hours at 1200°C in air clearly show the oxygen gettering effect of the γ phase (refer to Figures 14-18). A well defined selective oxidation zone (discrete $\alpha\text{-Al}_2\text{O}_3$ particles in a layer of unoxidized σ) was formed by alloys #1-#3. Alloy #4 (70 v/o σ + 30 v/o γ) did not form a distinct selective oxidation

zone. However, selective attack of the γ phase underneath the metal/scale interface in alloy #4 was evident. Alloy #5, which was single phase σ at 1200°C, suffered internal oxidative attack an order of magnitude greater in depth than the other alloys, all of which were at least partly γ .

Discussion of Nonprotective Oxidation Behavior at 1200°C in Air

The inability of $\sigma+\gamma$ alloys to form a continuous protective $\alpha\text{-Al}_2\text{O}_3$ layer is attributed primarily to the inherent limitations of a two phase microstructure. The aluminum-rich γ phase forms $\alpha\text{-Al}_2\text{O}_3$, but the σ phase does not. Activities of aluminum and niobium in the σ phase apparently are such that AlNbO_4 formation is favored over $\alpha\text{-Al}_2\text{O}_3$ formation. The establishment of a continuous $\alpha\text{-Al}_2\text{O}_3$ layer is interrupted because regions of the γ phase in the microstructure are physically separated from each other by the σ phase.

The predominant oxidation product at 1200°C is TiO_2 . Both the σ phase and the γ phase oxidize to form TiO_2 . Further, the microprobe data suggest that titanium diffuses faster at 1200°C than either aluminum or niobium. Therefore, it is not surprising that TiO_2 is the primary oxidation product and that a continuous $\alpha\text{-Al}_2\text{O}_3$ layer is not established.

1400°C

Nonprotective paralinear oxidation kinetics were observed for both alloy #6 and alloy #3 at 1200°C (Figure 19). The oxidation kinetics for alloy #3 remained paralinear at 1400°C, but at a higher rate of oxidation than that observed at 1200°C. However, protective parabolic oxidation kinetics were observed for alloy #6 at 1400°C. This result is consistent with the finding that the critical aluminum content needed for an Nb-Ti-Al alloy to exhibit protective parabolic oxidation kinetics at high temperature is 44 a/o (alloy #6 contained 50 a/o aluminum and alloy #3 contained 40 a/o aluminum) [1a].

Somewhat surprisingly, given its poor oxidation behavior, alloy #3 appeared to form a continuous inner $\alpha\text{-Al}_2\text{O}_3$ layer at 1400°C (Figure 20a). However, a very thick transient oxide, tentatively identified as TiO_2 containing niobium and aluminum, was also formed. In addition, several regions of accelerated attack which resulted from local breakdown of the inner $\alpha\text{-Al}_2\text{O}_3$ were observed on the surface of the alloy #3 test sample. Excessive transient oxidation and random breakdown of the $\alpha\text{-Al}_2\text{O}_3$ layer were the source of the poor oxidation behavior of alloy #3 at 1400°C.

The oxide scale which formed by alloy #6 at 1400°C consisted of a continuous inner layer of $\alpha\text{-Al}_2\text{O}_3$ plus a thin mixed outer layer of $\alpha\text{-Al}_2\text{O}_3$ and a transient oxidation product similar to that observed on alloy #3 (Figure 20b). Based on the TGA curves, the $\alpha\text{-Al}_2\text{O}_3$ layer formed by alloy #6 was protective.

The microstructures of alloy #3 after 30 minute and 24 hour exposures at 1400°C consisted of a fine uniform "basketweave" structure characteristic of decomposed β phase (Figure 21). Alloy #6 was therefore thought to be single phase β at 1400°C. This supposition is supported by the calculated 1400°C isotherm (Figure 2) and TEM analysis [2,4].

As-received arc-melted alloy #6 consisted almost entirely of the γ phase. Several small unidentified peaks were also present in the diffraction pattern. After 30 minutes exposure at 1400°C, alloy #6 remained primarily γ . Small amounts of the σ phase were also detected.

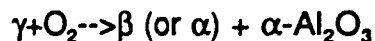
The microstructure of alloy #6 after 30 minute and 24 hour exposures at 1400°C consisted of an aluminum rich phase and a fine two-phase mixture (Figure 22). Based on the x-ray diffraction results and the calculated 1400°C isotherm, the aluminum rich phase was identified as the γ phase. The fine two-phase mixture was identified as the σ phase and a second region of the γ phase because only σ and γ were identified by x-ray diffraction.

The primary γ was significantly more coarse in the 24 hour exposure sample than in the 30 minute exposure sample. It was therefore concluded that the γ phase was present at 1400°C and retained at room temperature. The primary γ phase was also examined optically for evidence that it formed from a massive type transformation during cooling, however no such evidence was found.

The fine $\sigma+\gamma$ mixture appeared similar in both the 30 minute and 24 hour exposure samples. This suggests that the $\sigma+\gamma$ mixture was a decomposition product of a high temperature phase and formed during cooling. According to the calculated 1400°C isotherm, alloy #6 is single phase γ . However, the two-phase regions $\gamma+\eta$ (NbAl_3+Ti), $\gamma+\sigma$, $\gamma+\beta$, and $\gamma+\alpha$ fall near the composition of alloy #6. Because the decomposition product appeared to be aluminum lean in the SEM backscatter mode micrographs, the most likely candidates for the high temperature phase are the β phase or the α phase. Both the β and α phases are capable of decomposing during cooling to $\sigma+\gamma$. Further work is necessary to determine the phase equilibria of alloy #6 at 1400°C. Of importance for this study, however, is that at 1400°C alloy #6 clearly consists predominantly of the γ phase and not the β phase.

Proposed Oxidation Sequence at 1400°C in Air

A zone depleted of the primary γ phase was present underneath the $\alpha\text{-Al}_2\text{O}_3$ layer in both the 30 minute and 24 hour exposure samples of alloy #6. Only the fine $\sigma+\gamma$ mixture, which formed during cooling, was present in this region. The depleted zone was much larger in the 24 hour exposure sample than the 30 minute exposure sample. The depletion of the primary γ phase underneath the $\alpha\text{-Al}_2\text{O}_3$ layer implies that the main source of aluminum for the $\alpha\text{-Al}_2\text{O}_3$ layer was the γ phase. The selective oxidation of aluminum from the γ phase resulted in a phase transformation from the γ phase to the β (or α) phase according to:



The β (or α) phase then decomposed during cooling to the fine $\sigma+\gamma$ mixture. The supposition that the γ phase was the source of the protective $\alpha\text{-Al}_2\text{O}_3$ layer is supported by the oxidation behavior of single phase γ alloys, which oxidize to form a protective $\alpha\text{-Al}_2\text{O}_3$ layer at high temperature [8].

The average composition of the γ depleted zone was 29Nb-27Ti-44Al a/o. This composition corresponds to a borderline alloy composition needed to exhibit protective α -Al₂O₃ formation at high temperature. The average composition of the primary γ phase was approximately 25Nb-25Ti-50Al, which was the same as the overall bulk composition of the alloy. It is speculated that these compositions correspond to a tie line in the γ + β (or α) two-phase region at 1400°C. Alloys containing between 44 and 50 a/o aluminum (\approx 1:1 niobium: titanium ratio) fall in this two-phase region. Increasing the aluminum content from 44 a/o to 50 a/o increases the volume fraction of the γ phase in the microstructure. The formation of a primary γ depleted region underneath the α -Al₂O₃ layer suggests that the α -Al₂O₃ layer would not be maintained over long term exposures because the aluminum content of the γ depleted zone is borderline for α -Al₂O₃ formation.

Discussion of The Transition to Protective Oxidation Behavior at 1400°C in Air

The transformation of the microstructure of alloy #3 from σ + γ at 1200°C to single phase β at 1400°C contributes to the formation of a continuous α -Al₂O₃ layer. Aluminum is more uniformly distributed in the single phase β microstructure than the two phase σ + γ microstructure, and the β phase is capable of oxidizing to form α -Al₂O₃. Only the γ phase in the σ + γ microstructure is capable of oxidizing to form α -Al₂O₃. Diffusion of all alloy components (including aluminum) is more rapid at 1400°C than at 1200°C. An increase in the rate of aluminum diffusion would contribute to the formation of a continuous α -Al₂O₃ layer. However, alloy #3 is only a marginal continuous α -Al₂O₃ former at 1400°C and the oxidation kinetics are not protective because of excessive transient oxidation.

A transition to protective α -Al₂O₃ formation at high temperature in Nb-Ti-Al alloys is not observed until the aluminum content of the alloy is increased to greater than 44 a/o [1a]. The increase in aluminum content corresponds to the formation of the γ phase in the microstructure. The microstructure of alloy #6 at 1400°C consists of the γ phase and a small amount of a second high temperature phase, either β or α . A protective α -Al₂O₃ layer is formed on alloy #6 and the oxidation kinetics are parabolic.

CONCLUSIONS

An overview of preliminary attempts to define the roles of the σ , γ , and β phases during oxidation at 1200°C and 1400°C has been presented. Such information is thought critical for the development of oxidation resistant Nb-Ti-Al alloys, especially in terms of providing a basis for optimization of microstructure through processing. Based on the results of this study, efforts to develop oxidation resistant Nb-Ti-Al alloys should focus on single phase γ alloys or alloys which consist predominantly of the γ phase. If multiphase microstructures are necessary in order to optimize properties other than oxidation resistance, for example mechanical behavior, processing routes which modify the distribution of phases in the microstructure (for example the spacing between the σ and γ phases) may hold the potential for optimizing oxidation resistance. Finally, the key to successful development of oxidation resistant Nb-Ti-Al alloys, assuming such alloys are possible, is further advances in the understanding of phase equilibria in this system, which provides the foundation for systematic and intelligent experimental design and interpretation.

The following conclusions are drawn from this study for Nb-Ti-Al alloys exposed at 1200°C and 1400°C in air:

- 1) The transformation reaction from a β decomposed microstructure to $\sigma+\gamma$ is sufficiently fast that oxidation behavior is not affected.
- 2) The γ phase is the source of $\alpha\text{-Al}_2\text{O}_3$ and the σ phase is the source of AlNbO_4 formation in the oxide scales formed by $\sigma+\gamma$ alloys. Both phases oxidize to form TiO_2 .
- 3) The σ/γ interfacial area, the σ/γ volume fraction, and the continuity of the σ and γ phases in the microstructure influence oxidation behavior. Factors which increase the influence of the γ phase in the microstructure increase the resistance to oxidation.
- 4) The transition to protective alumina formation at high temperature is related to the γ phase and not the β phase.

REFERENCES

1. R.A. Perkins, K.T. Chiang, G.H. Meier, and R.A. Miller, "Effects of Alloying, Rapid Solidification, and Surface Kinetics on the High Temperature Environmental Resistance of Niobium", (Final Report Contract # F49620-86-C-0018 Air Force Office of Scientific Research, June 1989).
 - a) *ibid.*, p. 32.
 - b) *ibid.*, pp. 43-48.
 - c) *ibid.*, pp. 26-27.
2. U.R. Kattner and W.J. Boettinger, Materials Science and Engineering, A152 (1992) pp. 9-17.
3. J.H. Perepezko, Y.A. Chang, L.E. Seitzman, J.C. Lin, N.R. Bonda, T.A. Jewett, and J.C. Mishurda, in High Temperature Aluminides and Intermetallics, S.H. Whang, C.T. Liu, D.P. Pope, and J.O. Stieglwe, ASM/TMS-AIME, Metals Park, OH, 1990, p.19.
4. D.T. Hoelzer and F. Ebrahimi, in High Temperature Niobium Alloys, J.J. Stephens and I. Ahmad eds., TMS Warrendale, Pa. (1991), p. 105.
5. M.P. Brady, PhD. Dissertation, University of Florida, To be submitted August 1993.
6. D.T. Hoelzer and F. Ebrahimi: University of Florida, private communication (1991).
7. R.A. Rapp and G.N. Goldberg, "The Oxidation of Cb-Zr and Cb-Zr-Re Alloys in Oxygen at 1000°C", TAIME, 236, (1966) pp. 1619-1628.
8. C.S. Wukusick, "Oxidation Behavior of Intermetallic Compounds in the Nb-Ti-Al System", US Atomic Energy Commission Contract AT(40-1)-2847, General Electric Report GEMP-218, 31 July, 1963.

Table 1- Alloys Selected for Study at 1200°C

Alloy	Nominal Composition (atom %)	Predicted Phases	Observed Phases (± 5 volume %)
Alloy #1	15Nb-40Ti-45Al	Single-Phase γ	$\gamma + \alpha_2$ (small amount)
Alloy #2	23Nb-35Ti-42Al	"Majority γ " "Minority σ "	60 γ + 40 σ
Alloy #3	27Nb-33Ti-40Al	Equal σ and γ	55 σ + 45 γ
Alloy #4	32Nb-30Ti-38Al	"Majority σ " "Minority γ "	70 σ + 30 γ
Alloy #5	40Nb-25Ti-35Al	Single-Phase σ	100 σ

Table 2- Alloys selected for study at 1400°C

Alloy	Nominal Composition (atom %)	Predicted Phases	Observed Phases
Alloy #6	25Nb-25Ti-50Al a/o	γ	γ + small ?
Alloy #3	27Nb-33Ti-40Al a/o	β	β

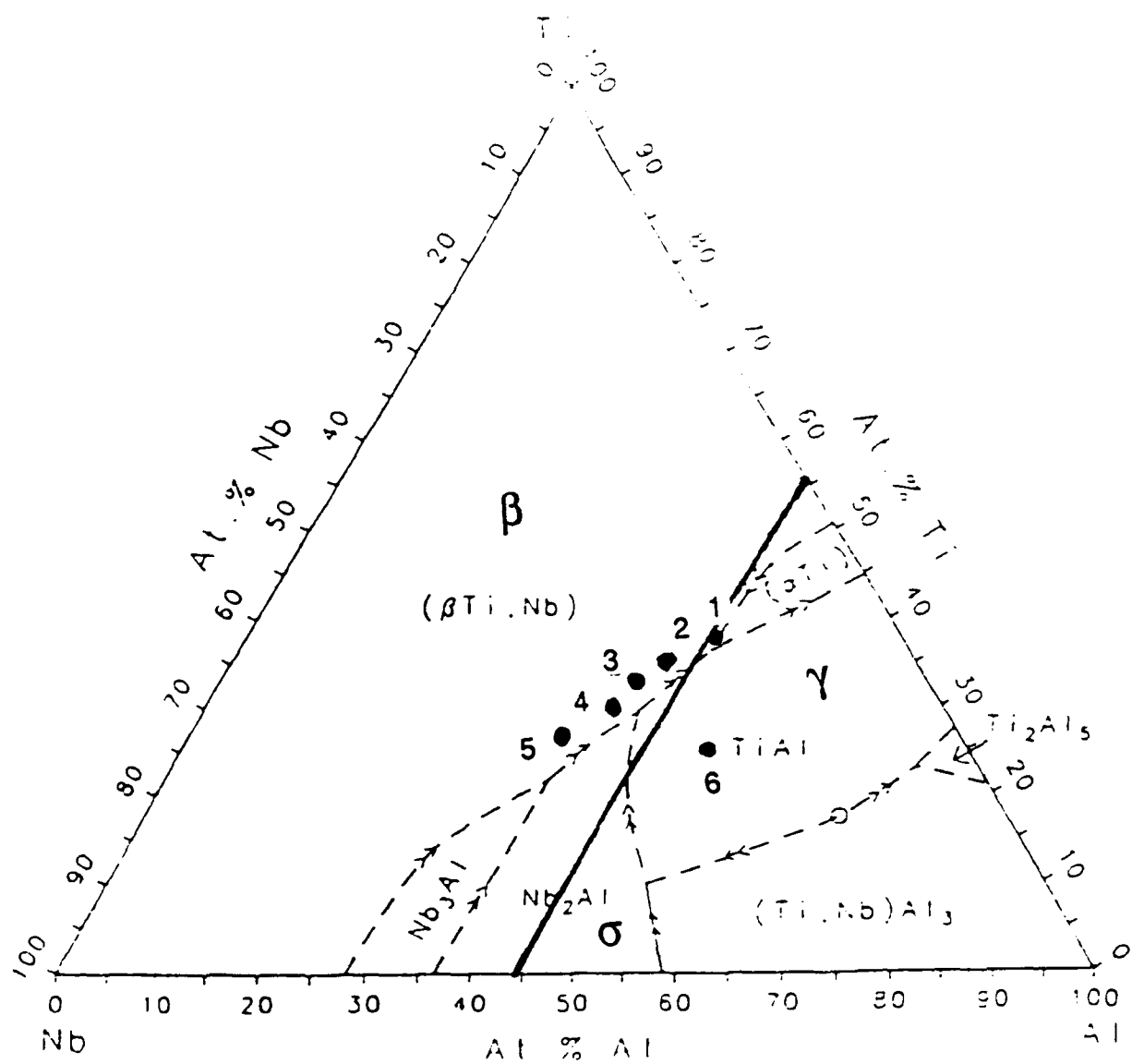


Figure 1- Preliminary Nb-Ti-Al liquidus projection (a/o) (Perepezko et al.) [3].

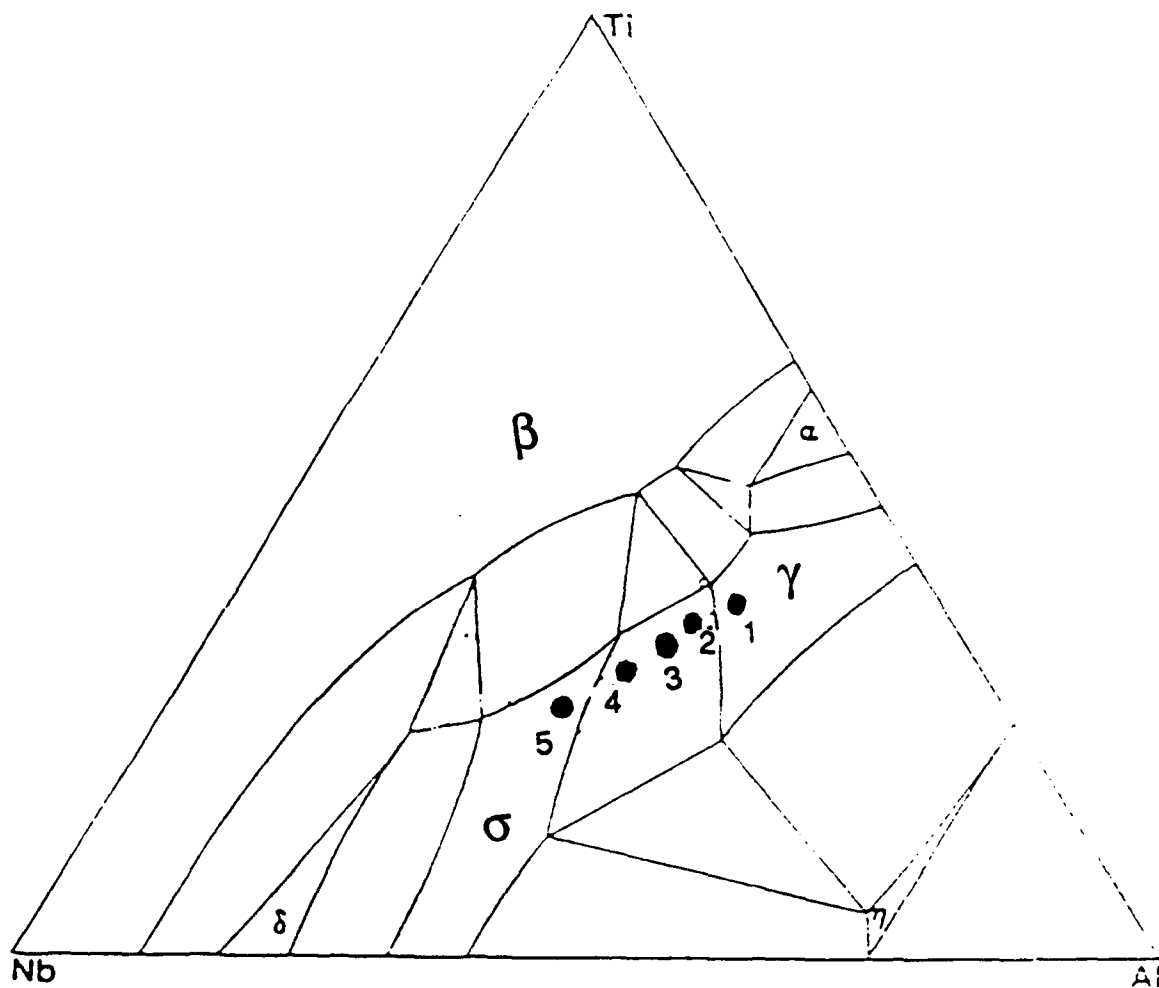


Figure 2- Isothermal Nb-Ti-Al section at 1200°C (a/o) (Hoelzer and Ebrahimi) [4]. Alloys #1-#5 fall on the same σ + γ tie line.

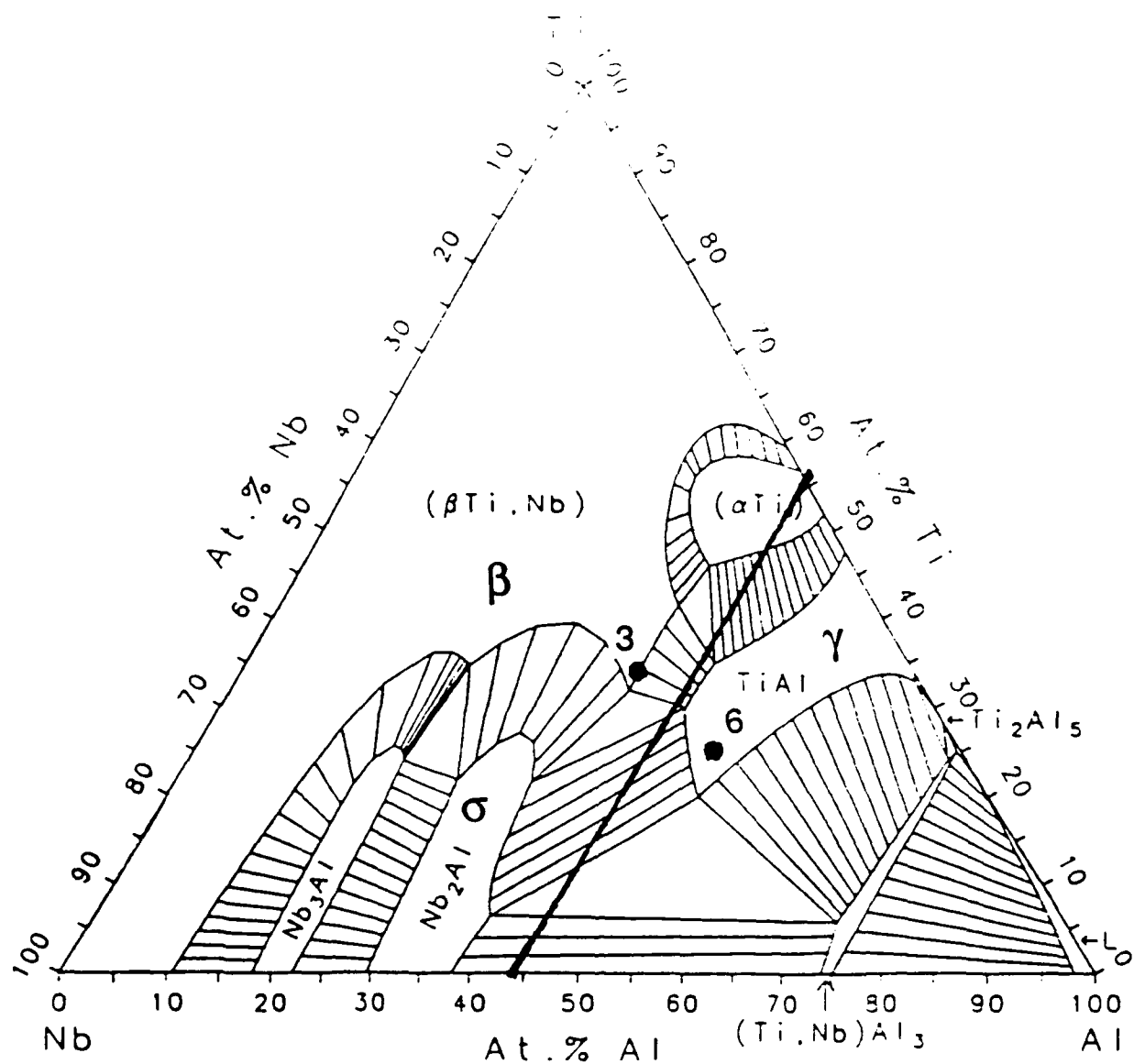


Figure 3- Calculated isothermal Nb-Ti-Al section at 1400°C (a/o) (Kattner and Boettinger) [2]. The minimum aluminum content needed to exhibit protective α - Al_2O_3 formation at 1400°C is 44 a/o (Nb:Ti = 1:1) [1a]. Note that this composition range coincides with the γ phase.

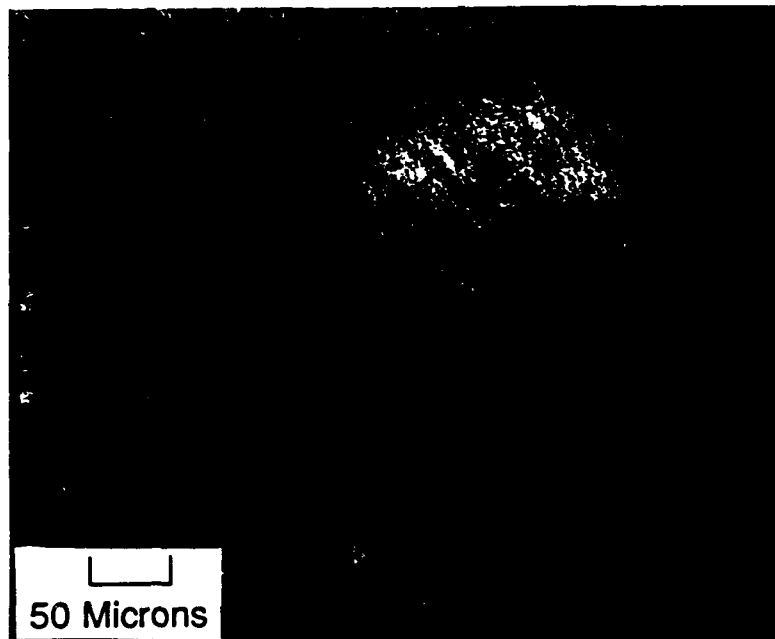


Figure 4- Optical micrograph of the arc-melted alloy #3 etched with Kroll's reagent. The prior β grains are extremely coarse. The matrix phases (β_2 , orthorhombic, ω -type, γ) cannot be resolved in this micrograph.

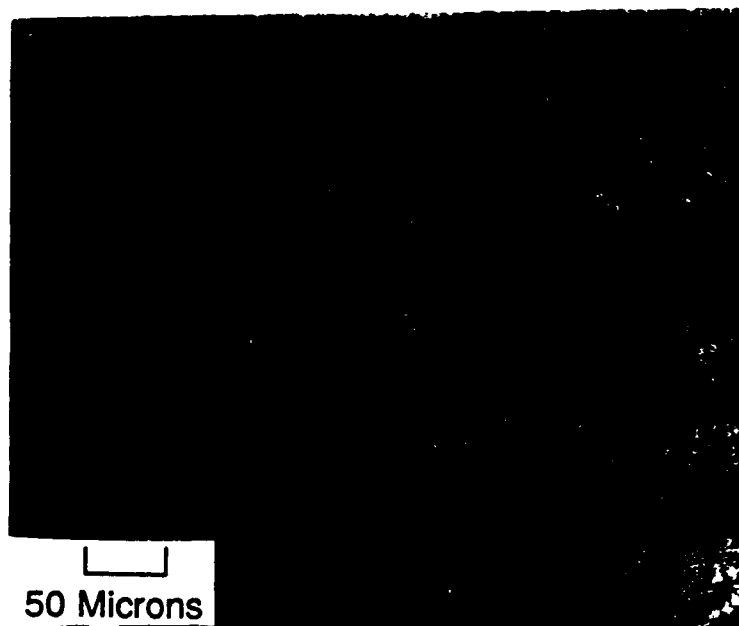


Figure 5- Optical micrograph of EML alloy #3 lightly etched with Kroll's reagent. The microstructure is β_2 with an orthorhombic phase precipitate. The matrix is under-etched to reveal the grain size.

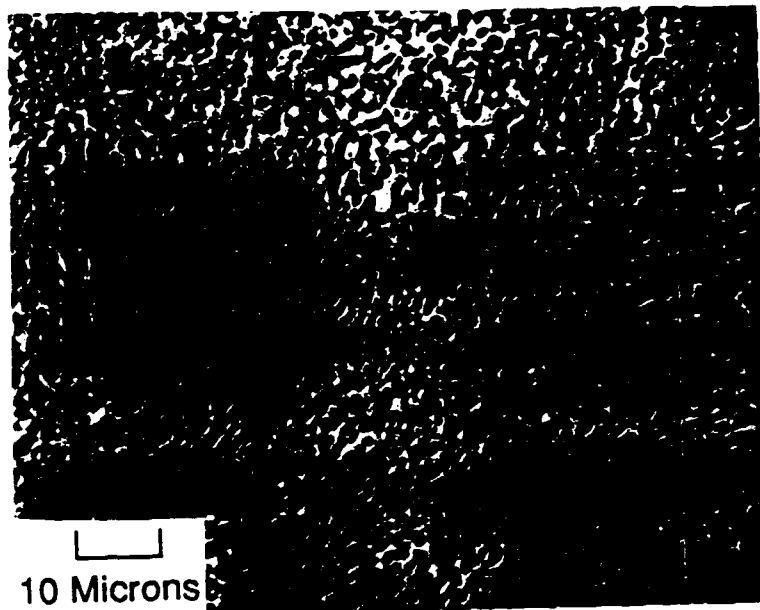


Figure 6- SEM (backscatter mode) micrograph of arc-melted/aged alloy #3. The microstructure consists of σ (light phase) and γ (dark phase).

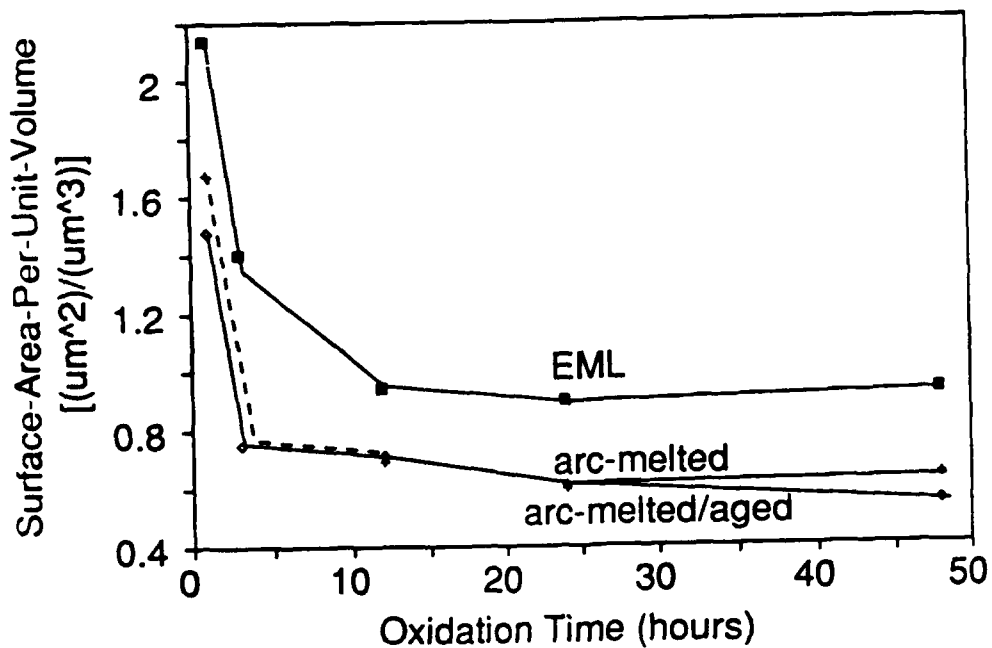


Figure 7- The $\sigma+\gamma$ microstructures of alloy #3 coarsen during the first 12 hours of exposure at 1200°C. The σ/γ interfacial area (described by the surface-area-per-unit-volume of the γ phase) is greatest for the test samples produced by EML (ie. finer microstructure).

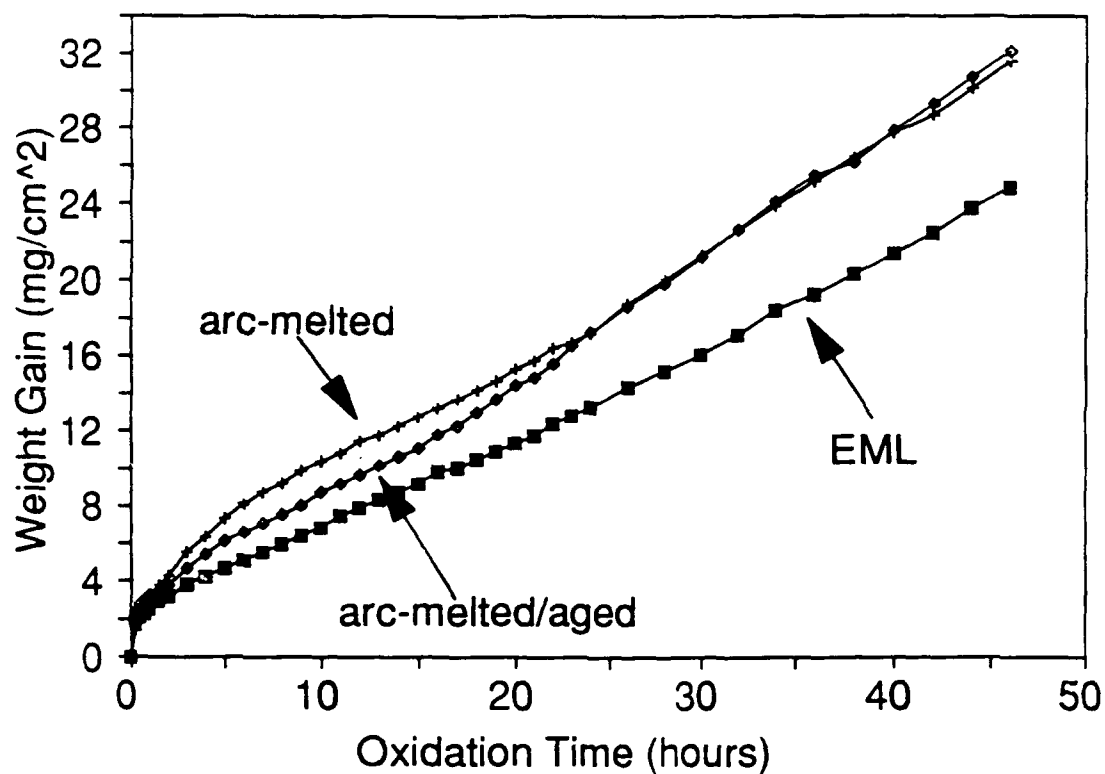


Figure 8- EML alloy #3 test samples exhibit the lowest rate of oxidation after exposure at 1200°C in air.

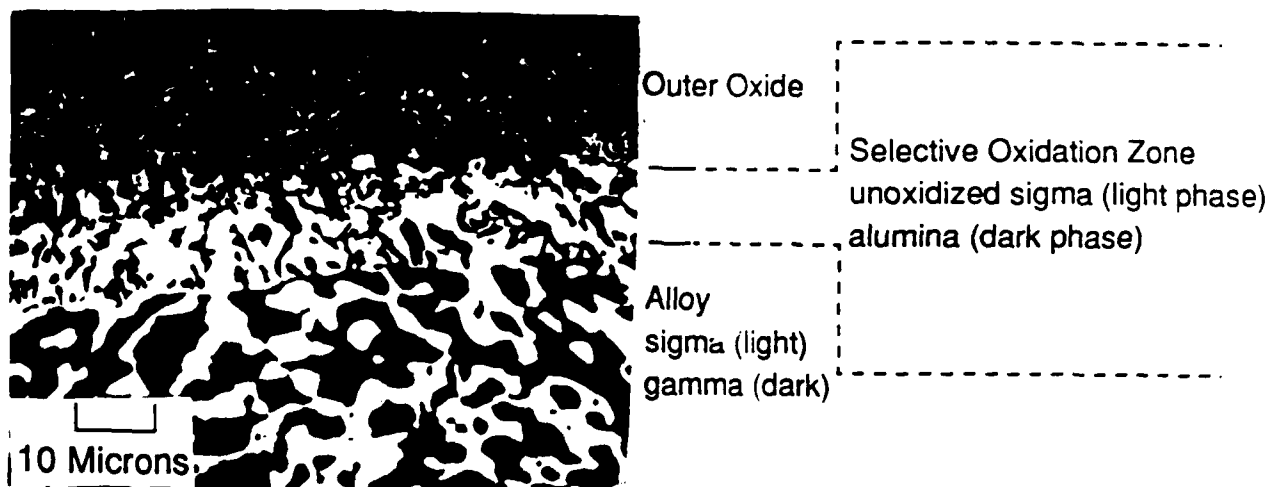


Figure 9- Typical SEM (backscatter mode) cross-section micrograph of alloy #3 exposed at 1200°C in air. The selective oxidation zone achieves a steady state thickness.

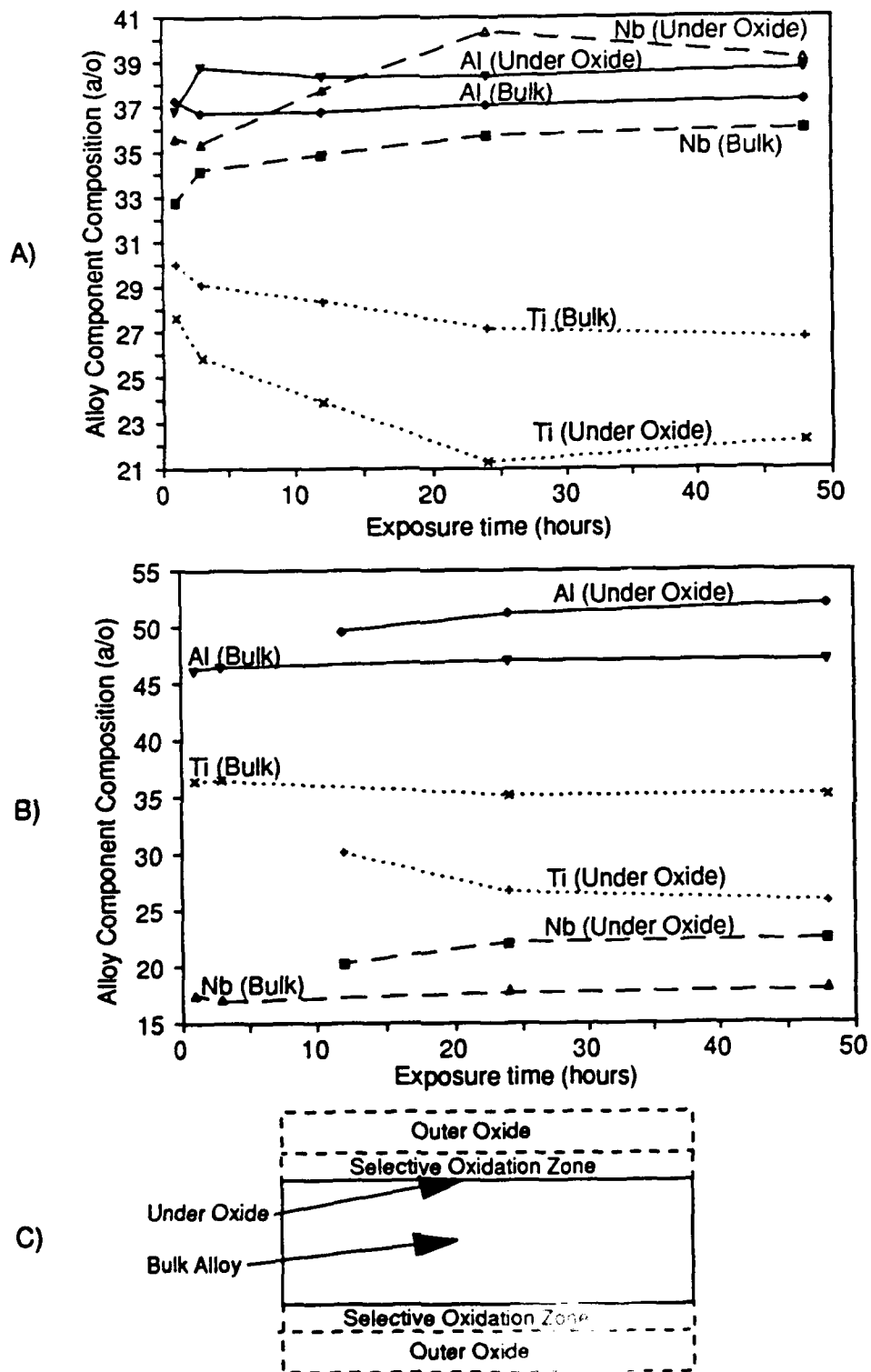


Figure 10- Titanium depletion and niobium and aluminum enrichment were observed underneath the growing oxide scale (measured in arc-melted alloy #3 exposed at 1200°C in air). Similar trends were observed for arc-melted/aged and EML alloy #3 a) σ phase b) γ phase c) Schematic sample cross-section showing locations of microprobe measurements

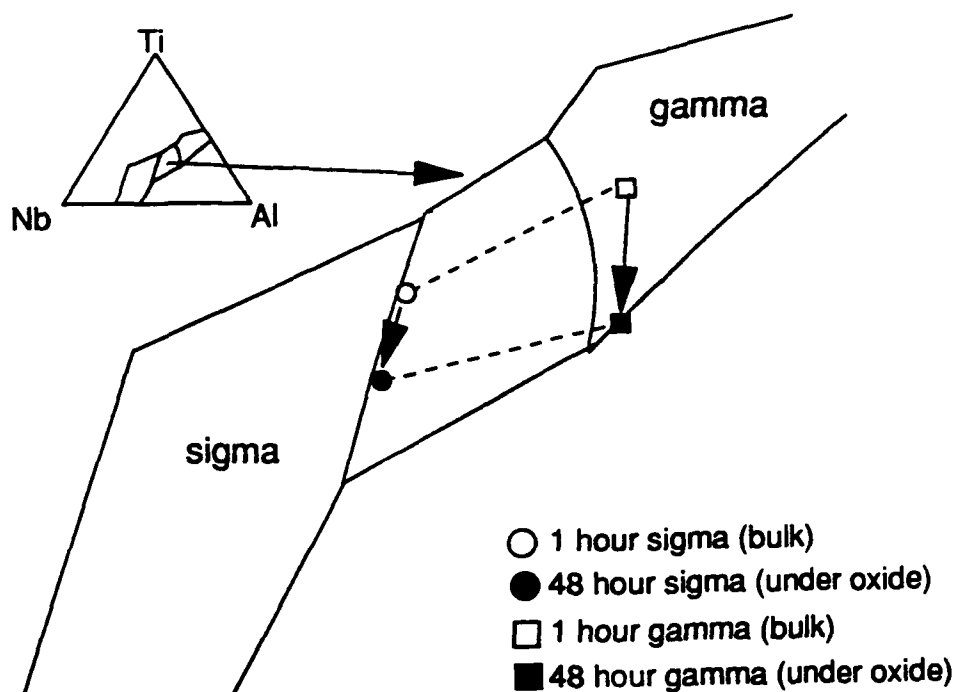


Figure 11- Microprobe data of Figure 10 plotted on the 1200°C isotherm shows that the composition of the alloy underneath the growing oxide scale moves away from the titanium rich corner of the phase diagram along the σ and γ phase boundaries.

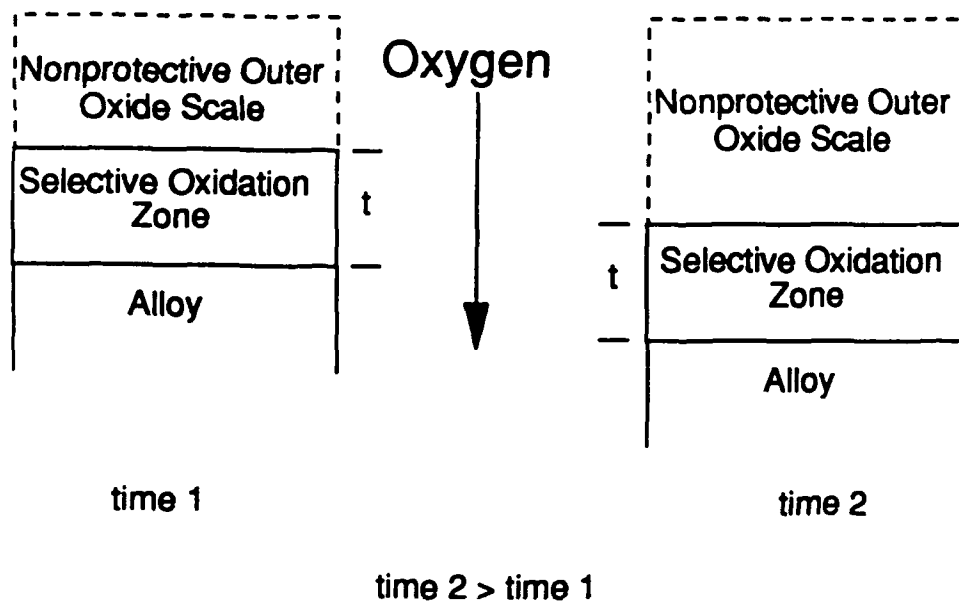


Figure 12- Schematic of proposed oxidation sequence for alloy #3 at 1200°C in air. The zone of selective oxidation achieves a steady state thickness.

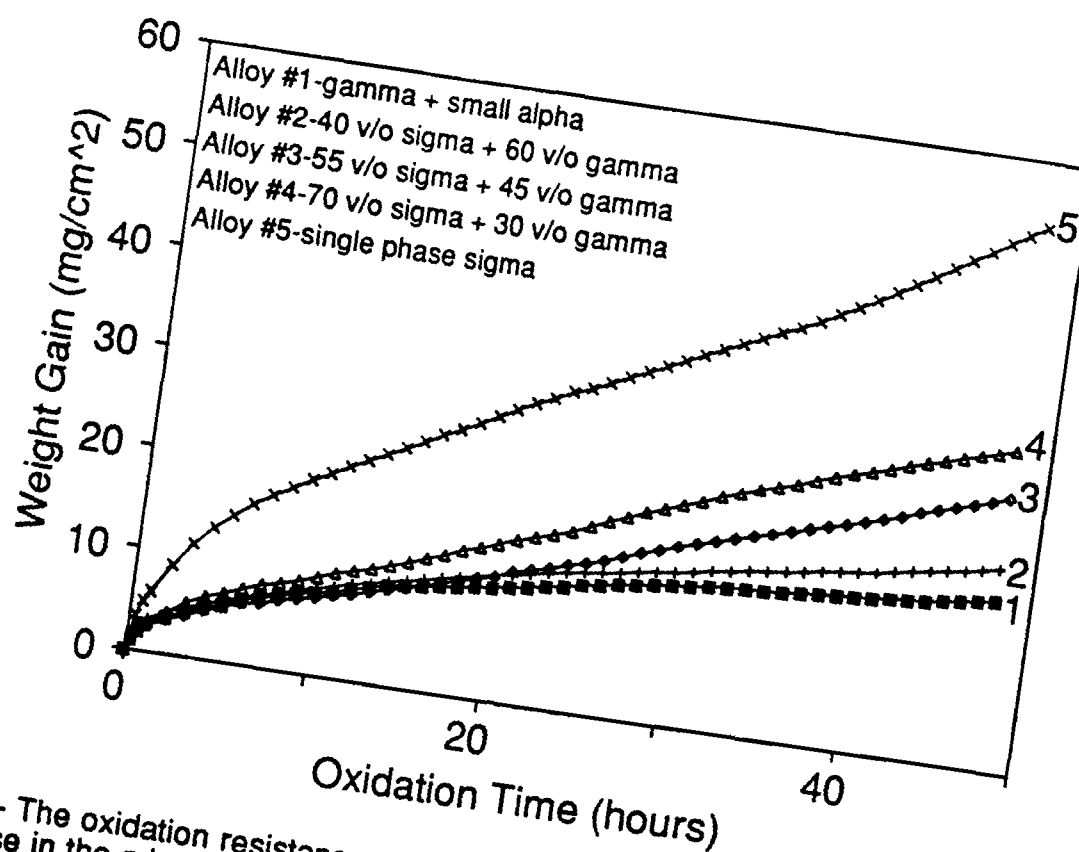


Figure 13- The oxidation resistance at 1200°C in air improves as the volume fraction of the γ phase in the microstructure is increased.

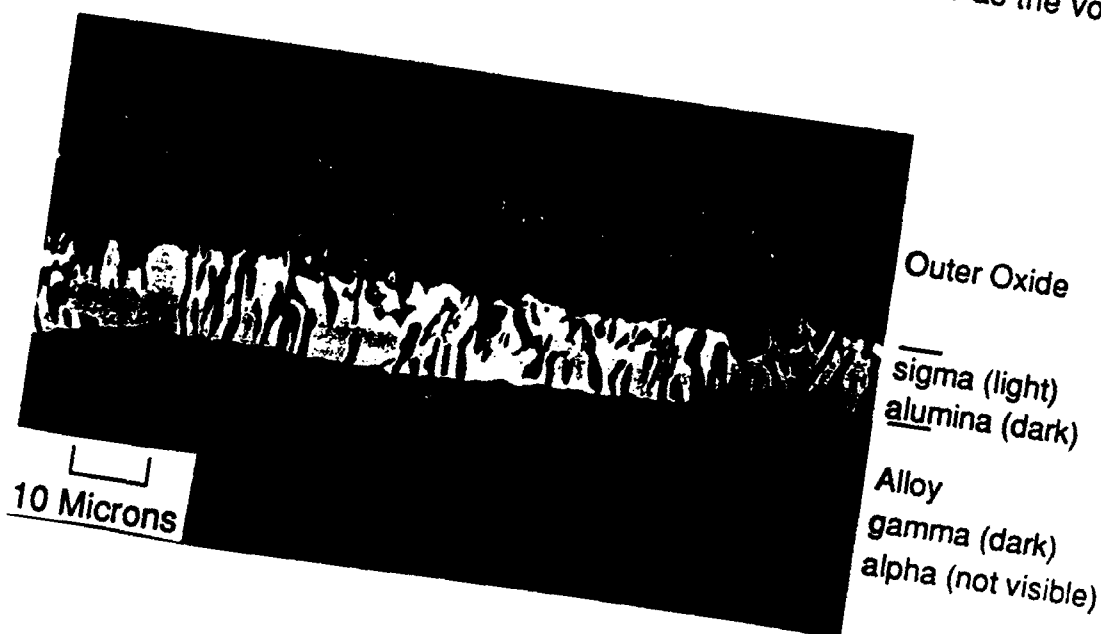


Figure 14- SEM (backscatter mode) cross-section micrograph of alloy #1 exposed for 48 hours at 1200°C in air.



Figure 15- SEM (backscatter mode) cross-section micrograph of alloy #2 exposed for 48 hours at 1200°C in air.

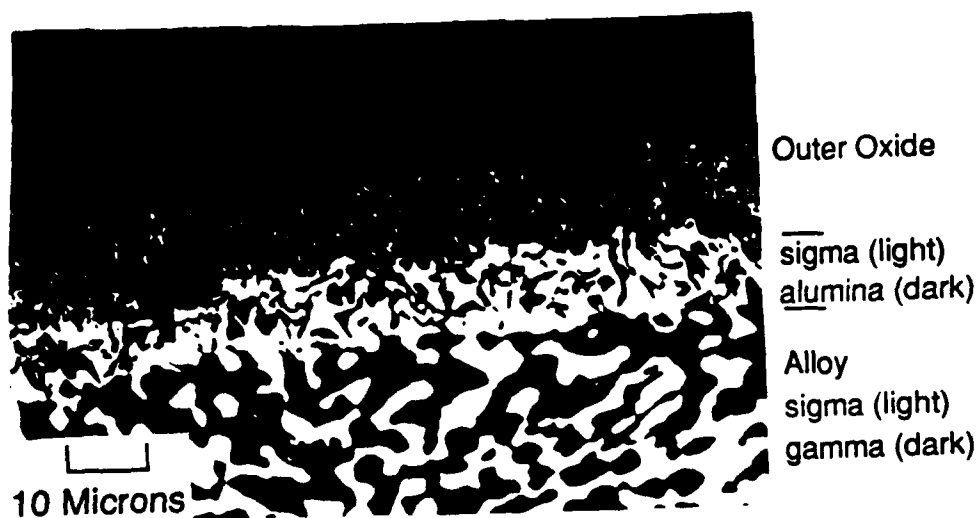


Figure 16- SEM (backscatter mode) cross-section micrograph of alloy #3 exposed for 48 hours at 1200°C in air.



Figure 17- SEM (backscatter mode) cross-section micrograph of alloy #4 exposed for 48 hours at 1200°C in air.

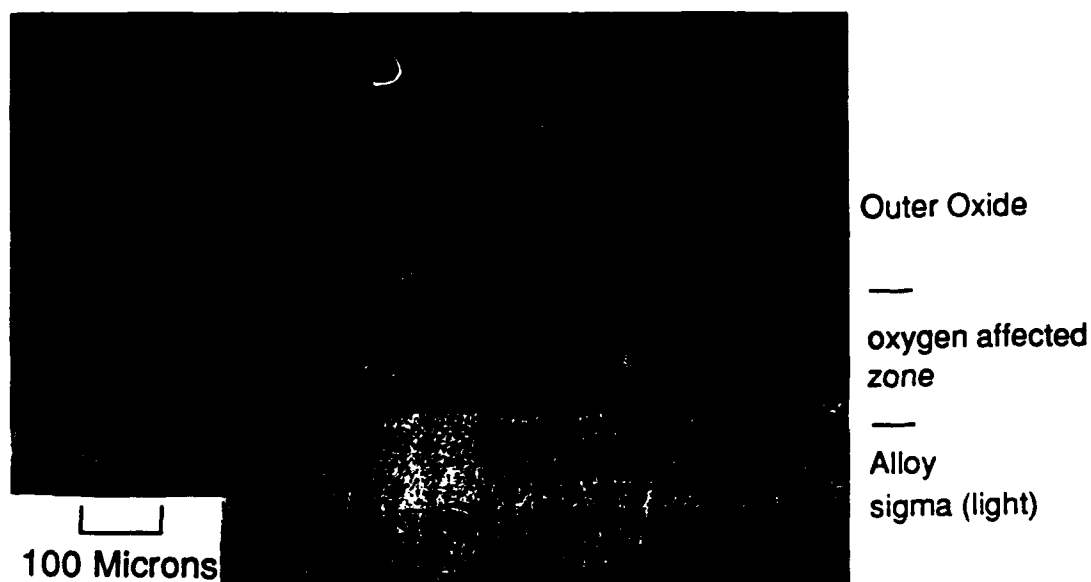


Figure 18- SEM (backscatter mode) cross-section micrograph of alloy #5 exposed for 48 hours at 1200°C in air.

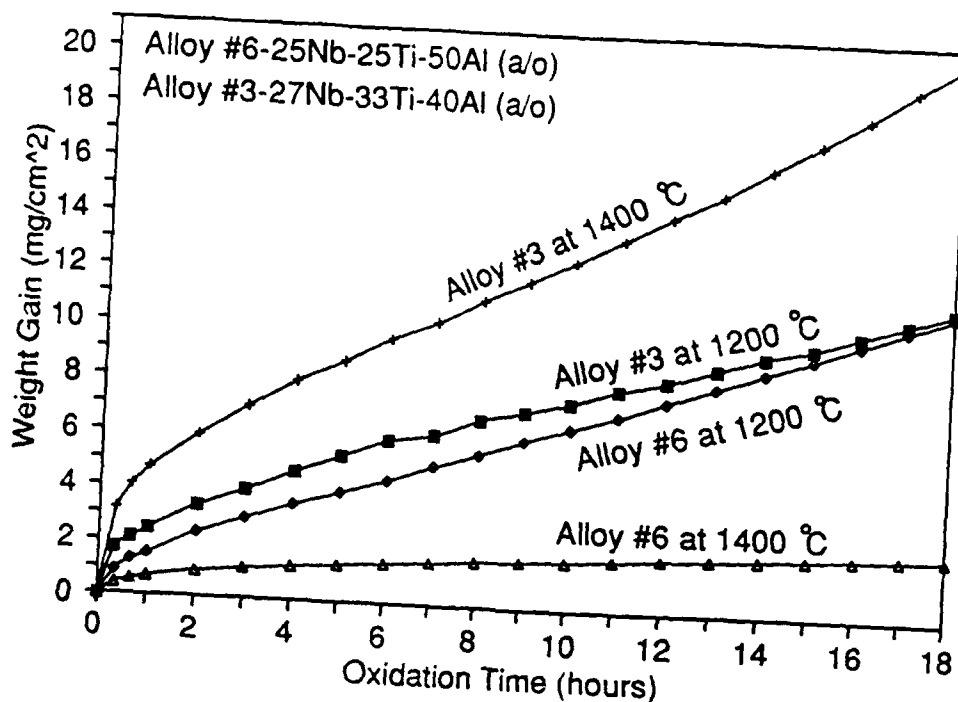


Figure 19- Alloy #6 exhibits a transition to protective oxidation behavior in air when the exposure temperature is raised from 1200°C to 1400°C. Alloy #3 does not.

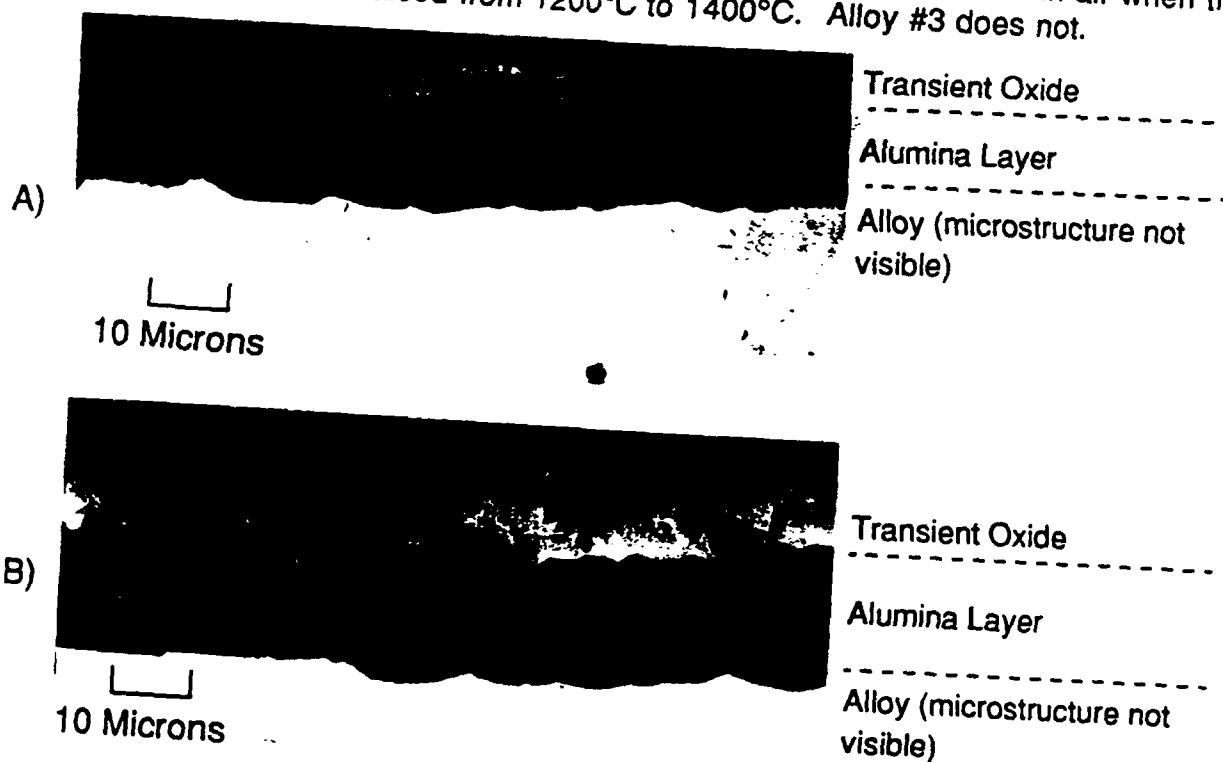


Figure 20- SEM (backscatter mode) cross-section micrographs of 24 hour 1400°C exposure samples showing the inner α -Al₂O₃ layer (dark) and the outer transient oxide (light). The transient oxide formed by alloy #3 is thicker than the transient oxide formed by alloy #6. a) Alloy #6 b) Alloy #3

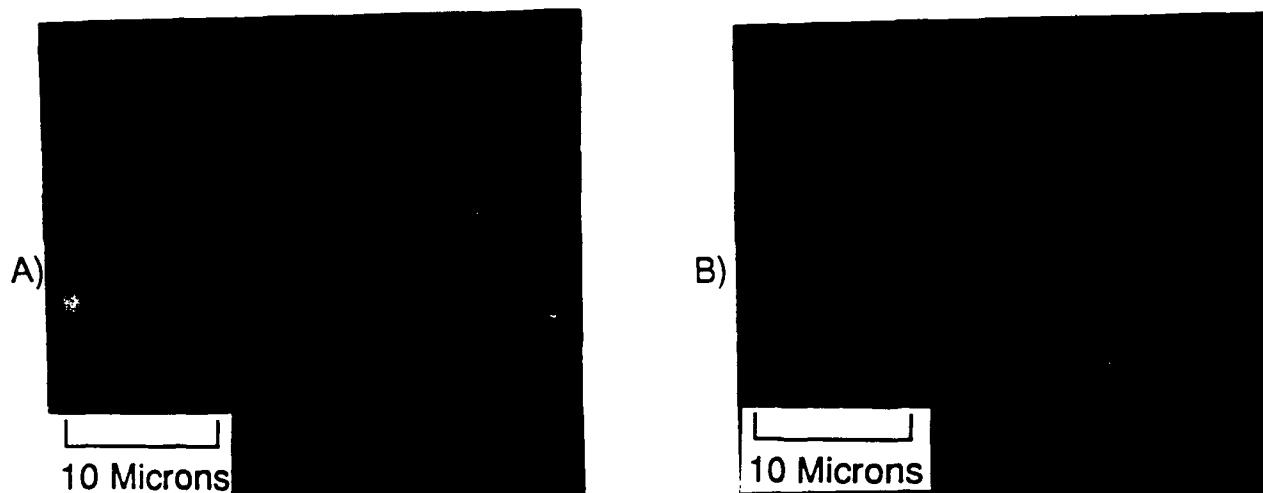


Figure 21- SEM (backscatter mode) cross-section micrographs of alloy #3 show the "basketweave" like morphology characteristic of decomposed β phase. a) 30 minutes (1400°C) b) 24 hours (1400°C)

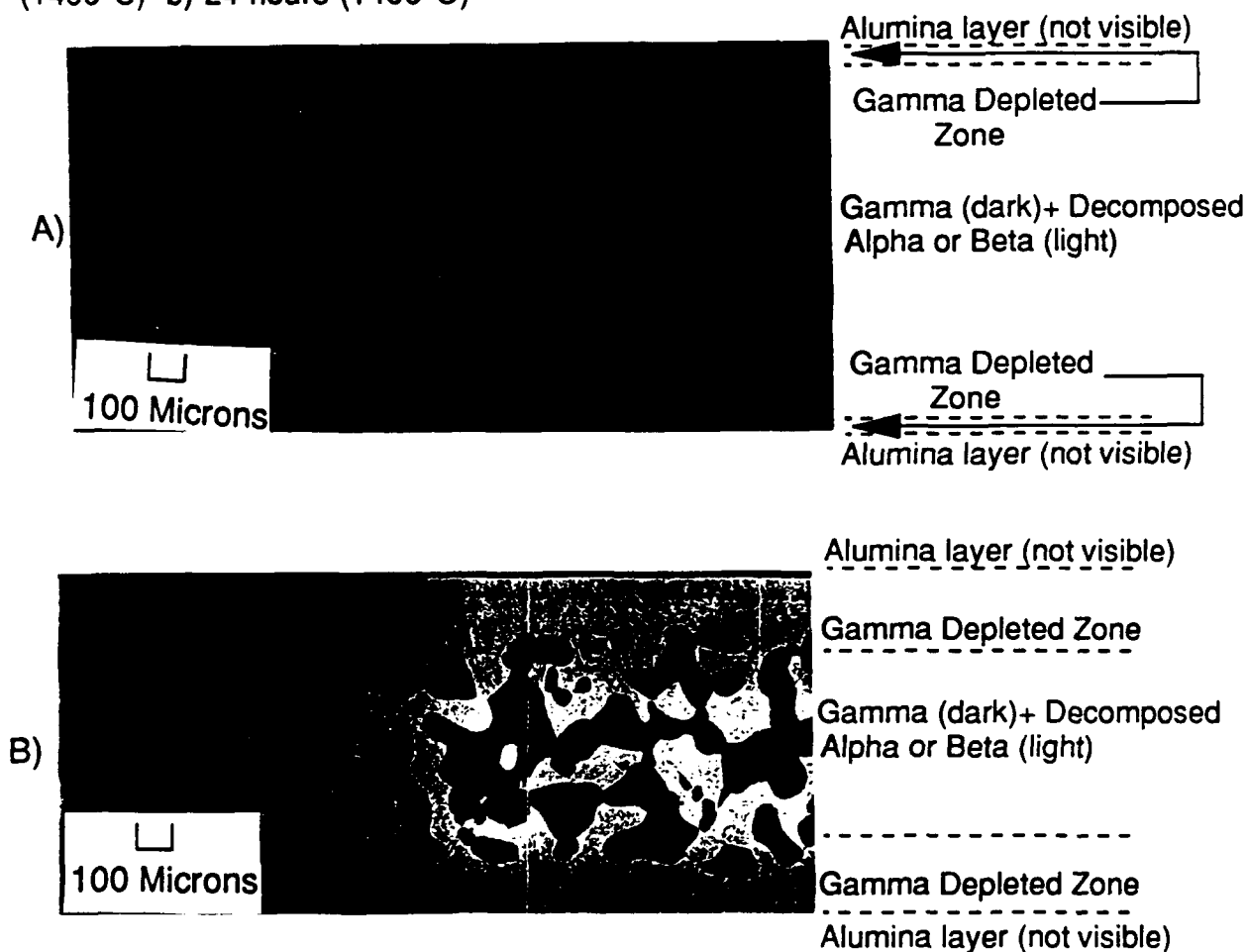


Figure 22- SEM (backscatter mode) cross-section micrographs of alloy #6 show that the microstructure consists of the γ phase (dark) and a fine $\sigma+\gamma$ mixture (light and dark). A γ depleted zone is present directly underneath the $\alpha\text{-Al}_2\text{O}_3$ layer. (The $\alpha\text{-Al}_2\text{O}_3$ layer is not visible in this micrograph). a) 30 min. (1400°C) b) 24 hours (1400°C)

EFFECT OF YTTRIUM IMPLANTATION ON THE OXIDATION BEHAVIOR OF Nb-25-Ti-25-Al-50 AT 1300° AND 1500°C.

R.J. Hanrahan Jr., M.P. Brady, E.D. Verink Jr. and S.P. Withrow*

145 Rhines Hall, University of Florida, Gainesville, Florida, 32611

*Oak Ridge National Laboratory, Oak Ridge, Tn. 37831

ABSTRACT

The effect of ion implanted yttrium on the oxidation behavior of Nb25-Ti25-Al50 was studied. Rectangular samples were implanted on two sides with 3×10^{15} ions/cm². Oxidation kinetics in air were studied using continuous thermogravimetric analysis. Exposures were conducted at 1300 and 1500°C for times ranging from 15 minutes to 144 hours. After exposure, samples were examined using X-ray diffraction, scanning electron microscopy, electron microprobe analysis, and Auger electron spectroscopy. No significant improvement in the implanted samples versus non-implanted samples was detected using any of these techniques. The lack of a reactive element effect (i.e. slower oxidation kinetics or improved scale adherence) in this alloy is attributed to a rapid initial transient oxidation period during which the implanted region is consumed by the advancing oxidation front.

INTRODUCTION

Due to the combination of low density and high melting temperature, alloys of the system Nb-Ti-Al are candidate materials for aerospace applications in high temperature oxidizing environments. Without the use of coatings, development of oxidation resistance is largely dependent on the formation of protective, adherent alumina layers by selective oxidation [1]. At very high temperatures, formation of alumina is favored; however, at somewhat lower temperatures formation of a non-protective layer of (primarily) titania is formed [2]. A process which reduces the kinetics of formation and/or increases adherence of alumina in these alloys would be of great value in investigating the mechanism of protective alumina formation as well as having potential engineering applications. Numerous papers have been published on the "reactive element effect" (REE) which qualitatively consists of improved scale adherence and reduced oxidation rates observed in various alumina or chromia forming alloys due to the presence of small quantities of a reactive element such as yttrium. [3] This effect is particularly effective in improving performance of alloys which form alumina but may also improve "marginal" alumina formers in some cases [4].

The alloy chosen for this study was 25-25-50 Nb-Ti-Al which is considered one of the most promising alloys in this system from an oxidation standpoint. An earlier survey of the effects of implantation of Y in 25-25-50 Nb-Ti-Al gave some indication that a positive result was produced. [5] The present study therefore consists of a detailed investigation of the effect of Y implantation on the oxidation of 25-25-50 Nb-Ti-Al at 1300° and 1500° C. These temperatures were chosen since they span the range of formation of continuous alumina (at 1500° C) versus formation of alumina in a Ti based oxide matrix at 1300°C.

EXPERIMENTAL METHODS

Alloy Preparation

The alloy was prepared as a 250 gram arc-melted button by United Technologies (Pratt and Whitney). Cross sectional microprobe analysis showed no significant macrosegregation in the button. Previous work on an alloy of similar composition prepared at the same facility revealed no change in oxidation behavior attributable to a homogenizing heat treatment so samples were cut from the button as recieved.[6]. Individual samples were (approximately 1 cm² by 1 mm) were cut from the ingot with a wafering saw. Each sample was then ground and polished to 1 micron using standard metallographic techniques.

Ion Implantation Procedure

All of the ion implantation was carried out at the Surface Modification and Characterization facility at Oak Ridge National Lab (SMAC-ORNL). A 170 keV ion beam with a current density of 0.2-0.4 $\mu\text{A}/\text{cm}^2$ was used. In all cases the dose implanted was 3×10^{15} ions/cm². The ion dose was determined based on the results reported in ref. 5. In most samples both faces were implanted. Four samples were implanted on one side only to allow post oxidation comparison of oxide thickness and composition on implanted and non-implanted faces of the same sample. Ion doses and implantation distribution were modeled using the PROFILE code.[7] The calculated ion distribution is shown in Fig. 1.

Oxidation Treatment

Oxidation tests were carried out in air at 1 atmosphere. A Cahn 2000 microbalance was used for continuous gravimetric analysis at 1500°C and a Cahn RG balance was used for the 1300°C exposures. Samples were suspended by a sapphire rod hooked through a 1 mm diameter hole drilled through the sample by electron discharge machining prior to implantation. The furnaces used were ATS series 3110 with Kanthal super "33" heating elements. The entire suspension apparatus was inside an alumina reaction tube (in the hot zone) joined by a glass tube to the balance. Samples were inserted into the furnace at temperature in order to reach exposure temperature as rapidly as possible. Samples are estimated to have reached the desired temperature in less than 1 minute. After the desired exposure duration, samples were removed from the furnace and allowed to cool to room temperature. Cooling took less than 10 min. Weight loss (if any) due to spallation on cooling was determined by comparing the final weight at the end of the exposure as recorded on the microbalance with the weight of the cooled sample. Up to four runs were made at both exposure temperatures for 24 hours both for implanted and non-implanted samples. This allowed variations in kinetics resulting from slight differences in implanted area or sample thickness to be averaged out as well as confirming the repeatability of measured kinetic data. Other exposures were run with durations varied from 15 minutes to 144 hours in order to study the development and growth of the oxide scale.

Electron and x-ray spectroscopy

In addition to the oxidation kinetics experiments described above, effects of implantation followed by oxidation on surface morphology have been studied using scanning electron

microscopy (SEM), and changes in both surface and cross-sectional composition have been monitored using electron microprobe analysis (EMPA). X-ray diffraction has been used to determine the crystallography of the oxide phases formed. Comparison of scale thickness and composition for implanted and non-implanted samples have been made using Auger spectroscopy (AES) and EMPA.

RESULTS and DISCUSSION

1300°C Exposures

Figure 2 shows TGA curves of both implanted and non-implanted samples oxidized at 1300°C. The data represent the results of several exposures. Although the curve for the implanted samples shows a slightly higher weight gain than the curve for the non-implanted samples, this variation is within the experimental error for the small number of samples exposed. Note that all of the samples exhibited a transition to linear oxidation kinetics after 4-6 hours of exposure. Linear kinetics are associated with the formation of a non-protective oxide scale. The weight gain remained linear for samples heated for up to 144 hours. Within experimental error the Y implantation has no effect on weight gain.

At 1300°C an undifferentiated and extremely porous, fine-grained oxide was formed. This can be seen in the secondary and backscatter images given in Fig.3. These micrographs were taken from samples exposed for 2 hrs. However the surface morphology of this oxide did not vary between exposures up to 144 hours, nor was any difference discernable between implanted and non-implanted samples. These results are characteristic of the oxidation of similar alloys at

temperatures between 800° and 1350° C. [8]

Powder X-ray diffraction analysis was performed on the spalled product from the sample surfaces and on the intact scales. X-ray diffraction was used solely for qualitative analysis of the oxide scales. After exposure at 1300°C small quantities of material spalled off the samples, primarily from the edges. After 144 hours of exposure one sample spalled off the entire oxide scale intact allowing comparison of the remaining interface with the bulk scale. In all cases the outer scale consists of a mixture of TiO_2 , AlNbO_4 , and Al_2O_3 . The inner scale consists primarily of Al_2O_3 and unoxidized sigma phase ($\text{Nb}_2\text{Al}+\text{Ti}$). A number of small peaks which could not be identified were also present in the diffraction patterns obtained from the inner scale. X-ray diffraction analysis of the scales formed on Nb-Ti-Al alloys is often complicated by broad and overlapping peaks which are characteristic of the oxides formed from these alloys. Complete characterization is often not possible, however, the major phases present in this scale were clearly identified.

Selected samples were mounted in Polymethylmethacrylate (PMMA) and cross sectioned (using a low speed diamond saw) for examination of the variation in elemental composition as a function of depth. Cross sectioned samples were polished to a 1 micron finish before examination. Quantitative electron microprobe analysis relies on the sample surface being smooth at dimensions finer than the beam size used for analysis. Due to difficulties with oxide porosity, which was particularly significant for samples oxidized at 1300°C, elemental analysis of the oxide scale must be regarded as only semi-quantitative. Nonetheless microprobe analysis does allow the comparison of many salient features of the implanted and unimplanted samples.

Figure 4 is a micrograph (400X) of a typical sample exposed at 1300°C for 72 hours. Note the

"banded" appearance of the oxide and the clear transition region, approximately 10 microns in thickness, between the oxide scale and the non-oxidized metal. Figure 5 presents higher magnification (1000X) of this transition region in non-implanted and implanted samples, each exposed for 72 hours. The thickness of the transition region is essentially the same in both samples. In fact the thickness of this layer was the same in all samples examined which had been exposed for more than 4 hours at 1300°C. Since diffusion across a layer of fixed thickness at a constant temperature occurs at a constant rate (assuming the oxide is saturated) the presence of this layer is believed to control the diffusion process and may account for the transition to linear kinetics observed after roughly 4 to 6 hours in all of the samples exposed at 1300°C.

Figure 6 shows compositional data from the oxide surface to the bulk metal taken at spacings of 3 microns on an implanted sample. The overall thickness and pattern of compositional variation is not modified by the Y implantation.

1500°C Exposures

Figure 7 presents averaged TGA results for implanted and non-implanted samples exposed at 1500°C for 24 hours. At this temperature implanted samples consistently gained less weight in the first few hours than non-implanted samples; however this difference disappeared at longer exposures. Oxidation at 1500°C produces a continuous alumina layer, as opposed to the mixed oxides formed at 1300°C, which leads to a considerably lower rate of weight gain.

The slower oxidation rate observed at 1500°C is likely attributable to the Y implantation, with the effect being lost when the oxide thickness had reached 10 to 100 times the implantation peak depth. This postulate is supported by Auger electron spectroscopy results from a Y-implanted sample exposed for 15 minutes. Figure 8 shows the Y and O concentrations versus depth into the

surface. Yttrium is detected in the near-surface region where it was implanted while the oxide had reached a thickness of more than 5000 angstroms during the 15 minute exposure. In the short term the Y may be reducing the oxidation rate by blocking oxygen diffusion pathways near the sample surface.

At 1500°C the oxide formed exhibited a definite grain structure, which coarsened as the duration of exposure increased. Figures 9 shows backscatter electron images of non-implanted and Y-implanted samples exposed for 72 hours at 1500°C. The dark phase is continuous and consists of essentially pure alumina while the light phase exists only at the outer surface of the sample and is a mixed oxide containing titanium and niobium. No significant difference in the phase distribution or grain size was observed between the implanted and non-implanted samples.

X-ray diffraction analysis of intact samples (oxide as-formed on the surface) exposed at 1500°C reveals that this scale consists primarily of α -Al₂O₃. A rutile (TiO₂) based oxide is also present. The Al₂O₃ is the dark phase shown in the surface SEM micrographs of Fig. 9. The results from XRD and from electron microprobe (discussed below) indicate that the light surface or transient oxide is TiO₂ with niobium-based oxides in solution, possibly TiO₂-NbO₂ or TiO₂-Nb₂O₅. In no case was any measurable difference found between the x-ray patterns of implanted and non-implanted samples. This is taken to mean that the Y implantation did not modify the overall mechanism of oxidation.

Figure 10 shows secondary electron images (SEI) of cross sectioned non-implanted and Y-implanted samples exposed at 1500°C for 72 hours. Note that the dark oxide is continuous, adherent, (and apparently the same thickness in both samples), and that the light oxide does not occur below the sample surface. Composition data taken every 10μ are plotted in Fig. 11.

Because of surface irregularities these data are only semi-quantitative. The important feature is that the oxide in both cases consists of continuous alumina in the bulk, and there is a sharp transition from the oxide to metal of the same composition as the bulk alloy.

As a further test of the effect of Y implantation on the thickness of the oxide scale formed, a sample which had been Y-implanted on one side only was oxidized for 6 hours at 1500°C and cross-section analyzed using EMPA. The mean of 14 measurements of the non-implanted scale was 18.2 μ while the mean of 18 observations on the implanted side was 18.83 μ . Since the spatial resolution of the microprobe is accurate to 1 micron, this variation is not significant. Hence the Y implantation does not have any measurable effect on scale thickness or composition on samples exposed for times from 1 to 72 hours.

CONCLUSIONS

No beneficial effect of implanting 25-25-50 Nb-Ti-Al with Y have been observed. The oxide scales formed at 1300°C spalled partially on cooling, whether on implanted or non-implanted surfaces, while scales formed at 1500°C were consistently adherent on both surfaces. Some limited reduction in oxidation kinetics was observed in the early stages of oxidation of samples at 1500°C. However the reactive element effect is not particularly noticeable in this study. This result is due to the initial rapid transient oxidation phase during which the implanted Y layer is consumed by an oxide which does not consist of continuous alumina. Insofar as this oxide appears to grow primarily by inward transport of oxygen anion, based on the implanted Y remaining near the surface, an ultimately similar result is expected even if higher doses or thicker implanted layers were employed.

ACKNOWLEDGEMENTS

Research at the Oak Ridge National Laboratory was sponsored by the Division of Materials Science, U.S. Department of Energy under contract DE-AC05-84OR21400 with Martin Marietta Energy Systems, Inc. We gratefully acknowledge the work of Dr. Eero O. Ristalainen in performing AES analysis for Y.

REFERENCES

- 1) R.A. Perkins and G.H. Meier "The Oxidation Behavior and Protection of Niobium", JOM, August 1990, P17-21.
- 2) C.S. Wukusick, U.S. Atomic Energy Commission Contract AT(40-1)-2847, General Electric Report GEMP-218 (31 July 1963)
- 3) M.J. Bennett "The Role of Ion Implantation in High Temperature Oxidation Studies", in High Temperature Corrosion, R. A. Rapp ed., NACE 1983.
- 4) R.A. Perkins, K.T. Chiang, G.H. Meier, and R.A. Miller "Effect of Alloying, Rapid Solidification, and Surface Kinetics on the High Temperature Environmental Resistance of Niobium" Air Force Office of Scientific Research Report LMSC-F352227, June 1989.
- 5) J.C. Liu, M.P. Brady, E.D. Verink Jr., and S.P. Withrow, "The Effect of Ion Implantation on the Oxidation Behavior of Nb/Ta Alloys at High Temperature", in High Temperature Materials Chemistry W.B. Johnson and R.T. Rapp eds., TMS 1990.
- 6) M.P. Brady, R.K. Stone, D.T. Hoelzer, S.P. Elder-Randall, and E.D. Verink Jr., "The Effect of Processing on the Oxidation Behavior of a Nb-Ti-Al alloy", in Processing and Manufacturing of Advanced Materials for High Temperature Applications, T.S. Srivatsan and V.A. Ravi eds. TMS 1992.
- 7) A.S. Armini and S.N. Bunker, Nucl. Instr. and Meth. in Phys. Res. B40/41 567 (1989).
- 8) M.P. Brady, R.J. Hanrahan Jr., and E.D. Verink Jr. "Oxidation behavior in the system Nb-Ti-Al", in Processing and Fabrication of Advanced Materials for High Temperature Applications II., T.S. Srivatsan and V.A. Ravi Eds. TMS 1993.

PROFILE calculation for Y implantation into NbTiAl

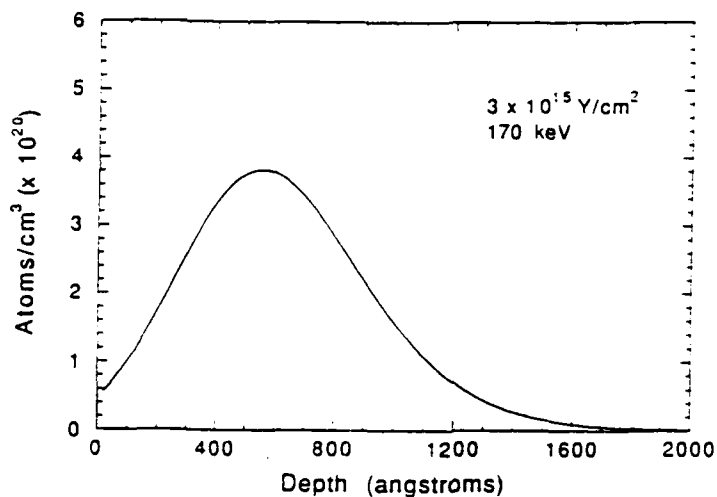


FIGURE 1: Calculated Y ion implantation distribution

TGA CURVES 1300 C

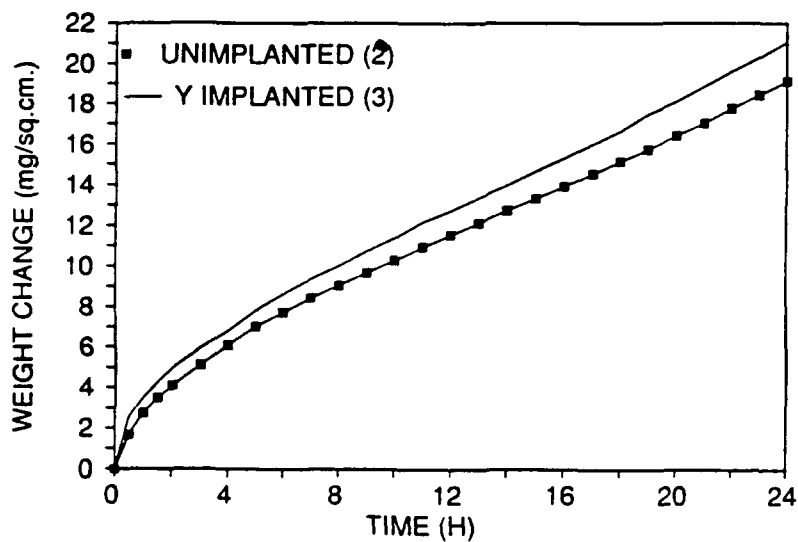


FIGURE 2: Results of continuous thermogravimetric analysis of samples exposed at 1300°C. Although the averaged Y-implanted samples show higher weight gain than the non-implanted samples, in individual samples both the highest and lowest weight gains were observed in non-implanted specimens.

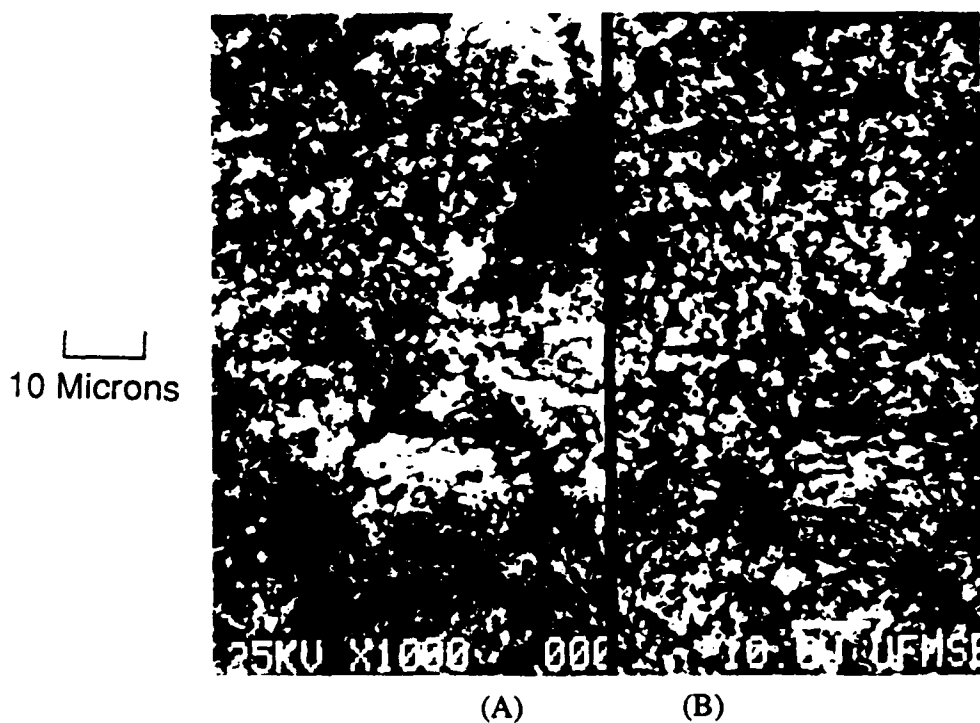


FIGURE 3: a) 400X Secondary electron image (SEI) of the surface oxide formed in air on 25-25-50 Nb-Ti-Al in 2 hours at 1300°C. This oxide scale is very porous and non protective. b) 400X Backscatter electron image (BSE) of the same surface as in a). Note that there is no apparent compositional variation. This scale is essentially titania containing Al and Nb.

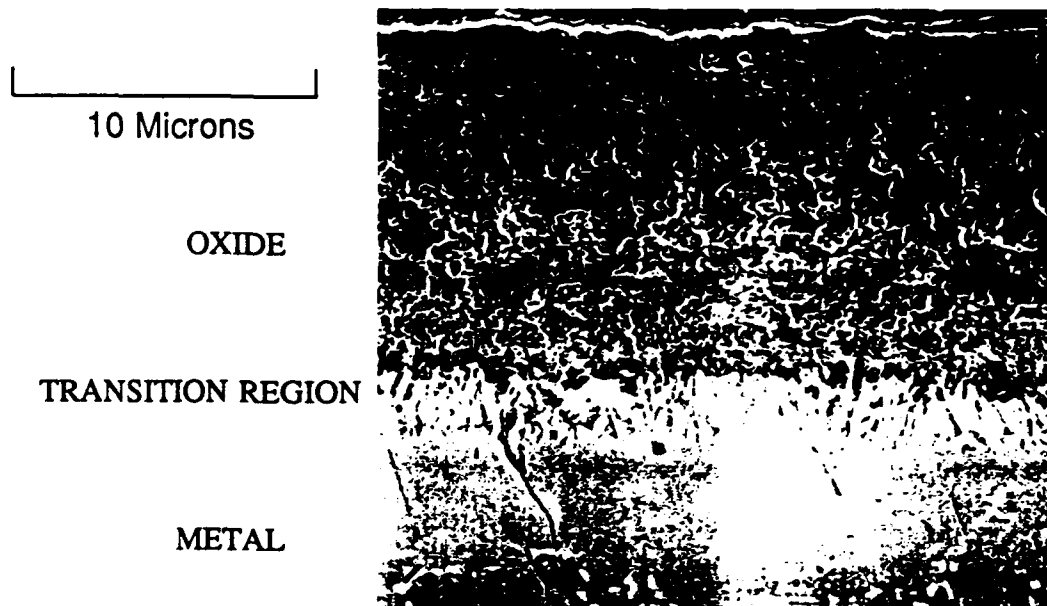


FIGURE 4: Secondary electron image (400X) of a cross section of sample exposed at 1300°C for 24 hours. Note the clear transition region between the outer scale and the underlying metal. This region appears to control the oxidation kinetics.

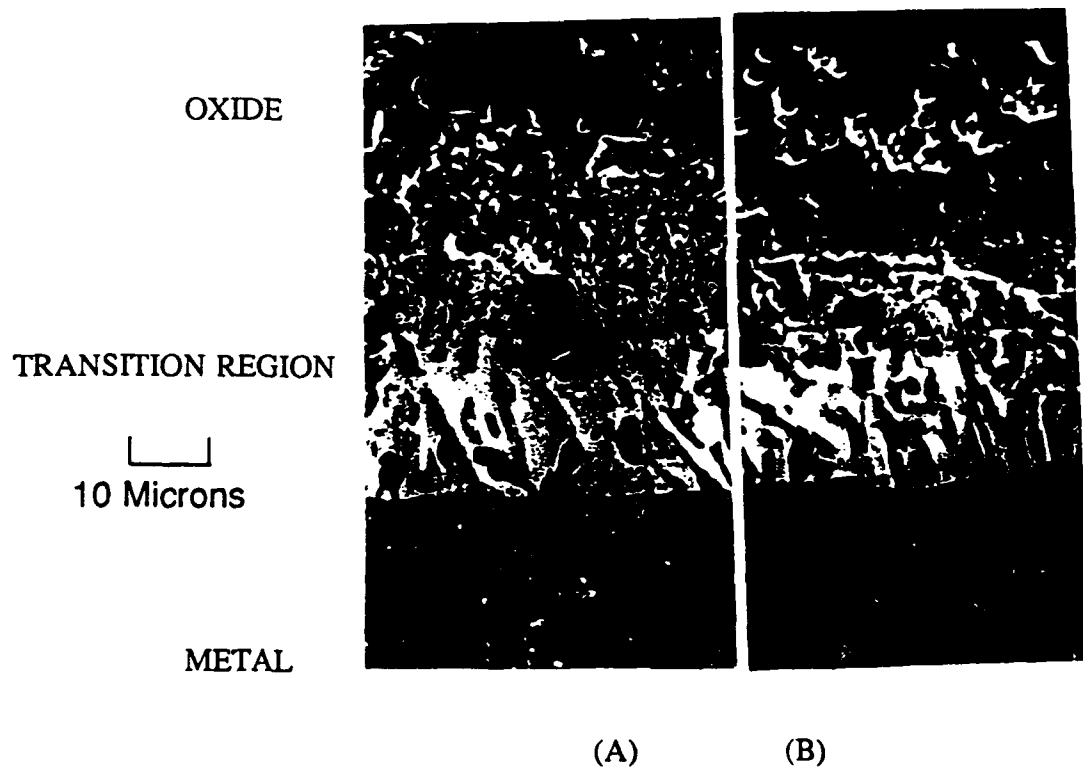


FIGURE 5: Secondary electron image (1000X) of cross section of a)non-implanted and b)implanted 25-25-50 Nb-Ti-Al alloy exposed for 24 hours at 1300°C. Note the characteristic banded oxide and the clear transition region between the oxide and remaining metal which is the same thickness in both cases. This zone of constant thickness appears to control the parabolic oxidation kinetics observed in these samples.

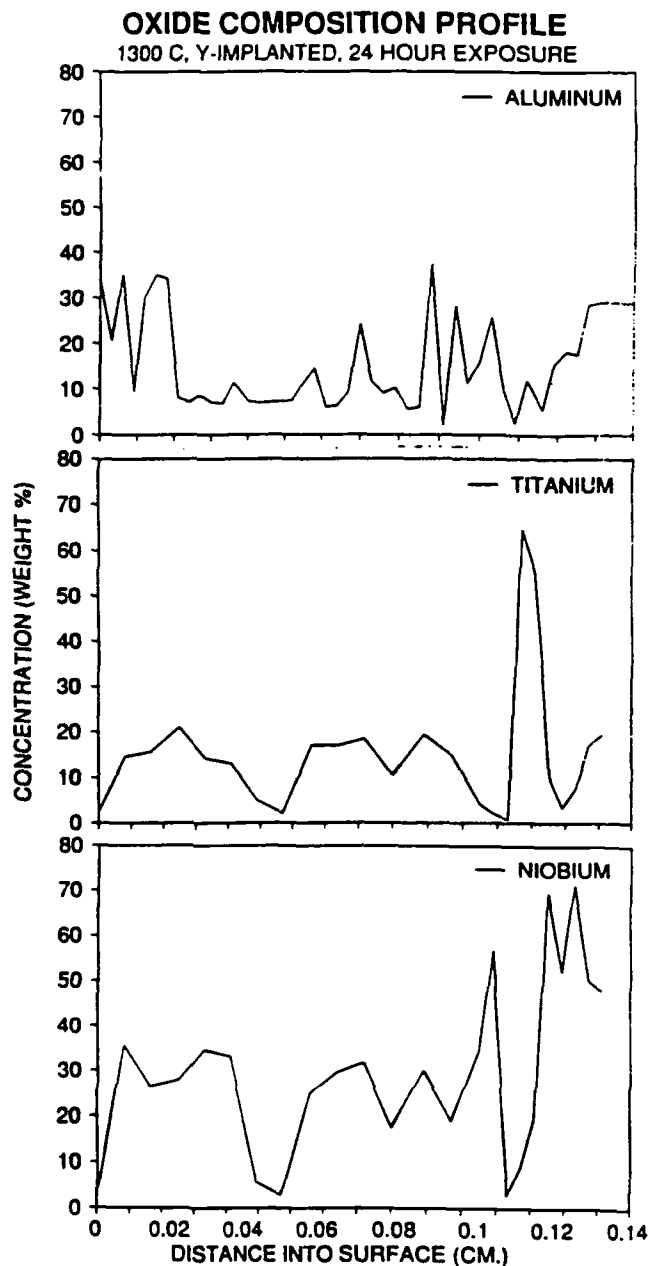
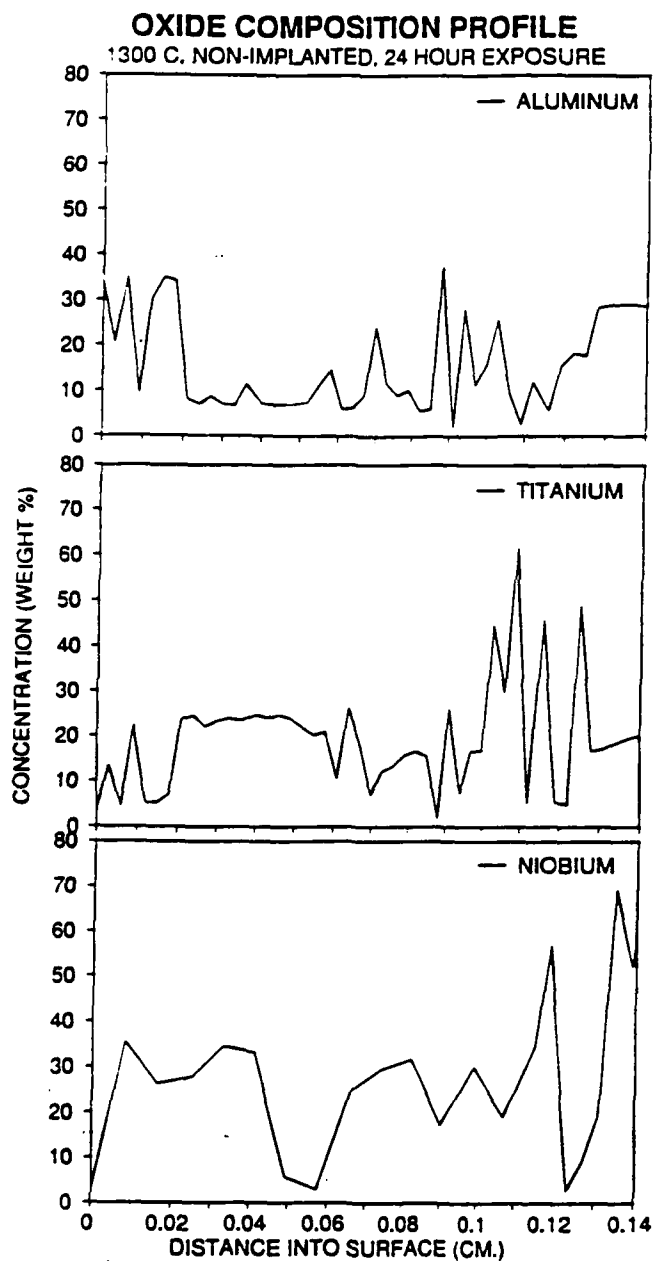


FIGURE 6: Compositional variation of scale on a) non-implanted and b) implanted 25-25-50 Nb-Ti-Al alloy exposed 24 hours at 1300°C. Although only semi-quantitative these data show the compositional banding characteristic of oxides formed in air at 1300°C on the 25-25-50 Nb-Ti-Al alloy.

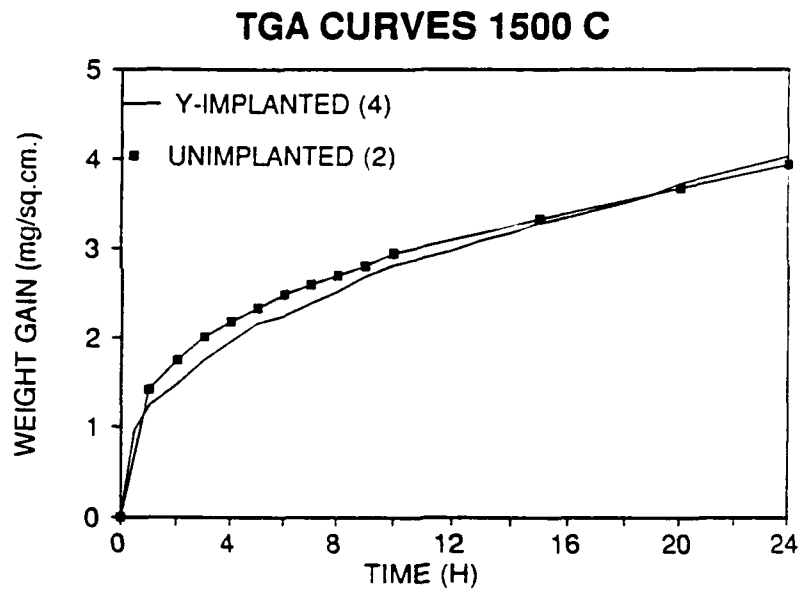


FIGURE 7: Results of thermogravimetric analysis of samples exposed for 24 hours at 1500°C. These curves are the average of several runs.

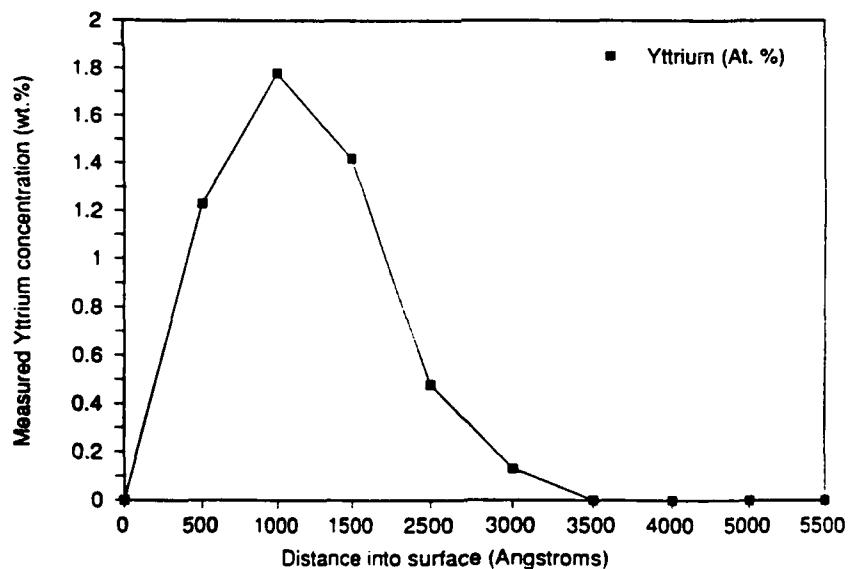


FIGURE 8: Distribution of Yttrium in the surface oxide on a sample exposed for 15 minutes at 1500°C, measured using Auger spectroscopy (AES). The Y has not moved from the near surface region where it is implanted. The broadened distribution, in comparison to Fig. 1, may be attributed to the rough surface finish - a 1 micron diamond polish is considerably rougher than the resolution of the AES. The peak broadening is therefore due to Y being implanted in 1 micron deep "valleys".

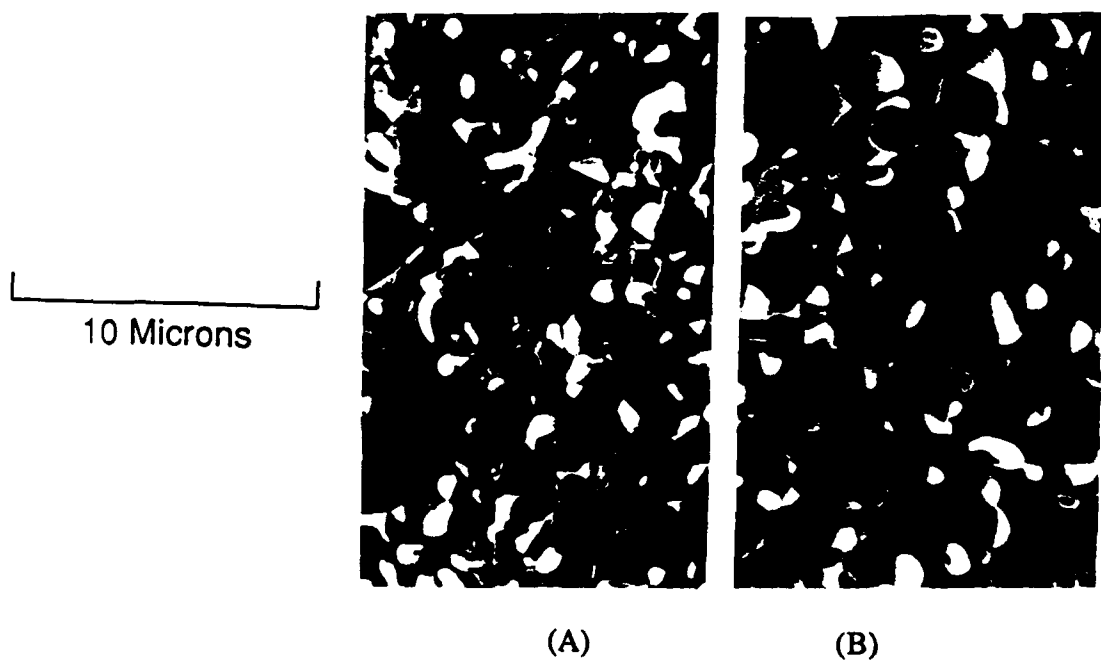


FIGURE 9: Backscatter electron image (400X) of a surface of a) non implanted and b) Y-implanted sample exposed for 24 hours at 1500°C. The coarseness of the oxide and the distribution of the white (TiO_2 based) transient oxide is the same in both cases.

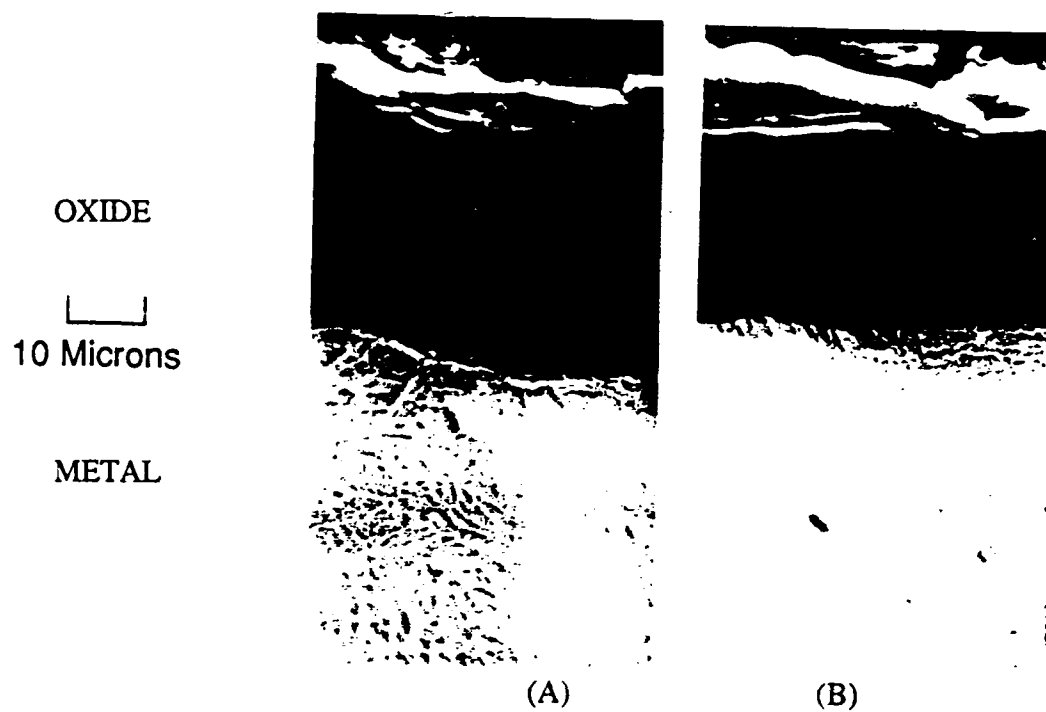
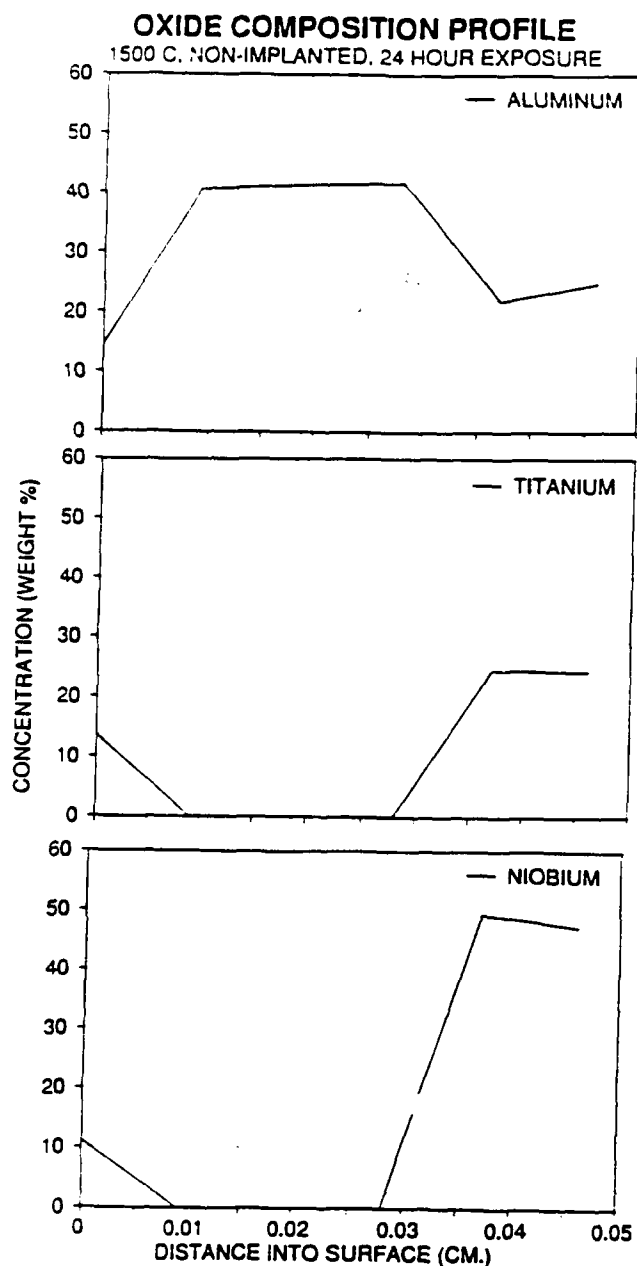
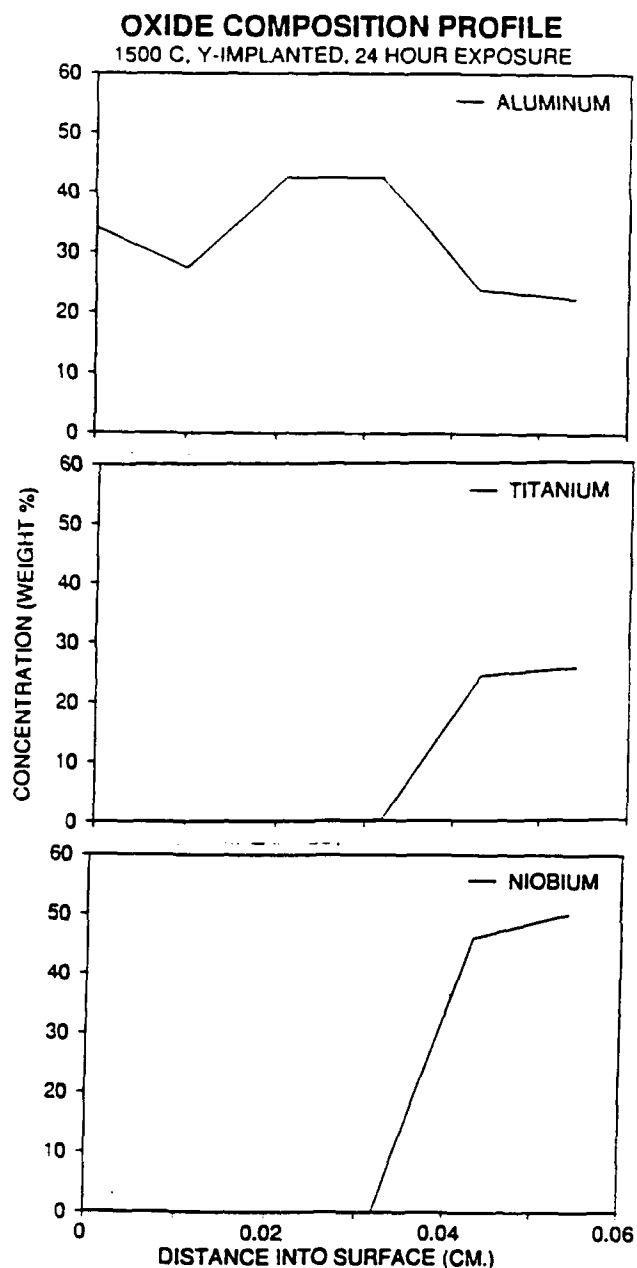


FIGURE 10: Secondary electron image (1000X) of a cross section of a) non-implanted and b) Y-implanted alloy exposed for 24 hours at 1500°C. The oxide appears black. Note that the thickness of the oxide in the non-implanted sample is essentially the same as in the Y implanted sample



(A)



(B)

FIGURE 11: Compositional variation of scale formed on a) non-implanted and b) Y-implanted alloy exposed for 24 hours at 1500°C, measured using EMPA. In the bulk the composition is primarily an aluminum oxide.

FRACTURE TOUGHNESS OF σ + α MICROSTRUCTURES IN THE Nb-Ti-Al SYSTEM

F. Ebrahimi¹, D. T. Hoelzer¹, and J. R. Castillo-Gomez²

¹Materials Science and Engineering Department, University of Florida,
Gainesville, Florida 32611

²Lagovan, S. A., Subsidiary of Petroleos De Venezuela
Maracaibo, Venezuela

Submitted to the journal of Materials Science and Engineering A
December 1992

Abstract

The Nb-Ti-Al system offers many intermetallics that can be potentially used for high temperature structural applications. The objective of this study has been to improve the room temperature toughness of the σ phase ($\text{Nb}_2\text{Al}+\text{Ti}$), which has a high melting point and good high temperature strength, with inclusion of semi-ductile phases. The incorporation of second phase particles have been found to enhance the toughness of the σ phase considerably. Fractographic analysis has revealed that when the interface between the particles and the matrix is strong, the second phase particles impede the crack front by trapping the crack tip due to plasticity. The crack propagation continues by a reinitiation process ahead of the crack tip. Consequently, the crack is bridged by the second phase particles. The cleavage of the second phase particles results in the final separation of the crack faces. In the case of weakly-bonded particles, the level of internal stresses has been found to influence the crack path, and therefore, the toughness. In this paper the effects of the volume fraction, size and distribution of the particles, as well as their nature on the fracture path and toughness are discussed.

Introduction

There has been a recent interest in developing advanced materials for high temperature structural applications. Most monolithic materials that have acceptable high temperature properties are very brittle at room temperature. Therefore, the aim of many investigations has been to architect multiphase materials, including composites, whose microstructures are optimized for a combination of high temperature mechanical response, such as creep resistance, and room temperature fracture toughness.

Many mechanisms have been identified to contribute to the toughening of brittle materials containing second-phase particles. The impediment of crack growth owing to the interaction of a crack front with particles has been explained by a mechanism similar to dislocation interactions with obstacles [1]. When a crack front is pinned by an array of obstacles, it bows out in the crack plane and between the second-phase particles, and the toughening is achieved due to an increase in the length of the crack front. This model suggests that the increase in toughness should correlate with the effectiveness of particles in pinning the crack front and the inter-particle spacing.

Crack deflection due to crack interaction with particles, whiskers, or fibers has been observed in composites [2]. Toughening arises whenever the particle crack interaction causes the deflection of the crack on a path that makes the crack to experience a low applied stress intensity factor (or crack driving force) than the maximum possible value. For example, in a polycrystalline material that is loaded in mode I, the crack deflects from the maximum stress intensity path and follows the easy fracture paths in each grain. In dispersion toughened materials the residual stresses, the image forces and the existence of weak interfaces provide incentive for crack deflection. It should be noted that crack

deflection does not by itself constitute a gain in toughness. An intergranular fracture path induced by weak grain boundaries may result in a lower toughness than a less deflected transgranular path. It is the balance between the weakness of the path and the degree of deviation from the maximum energy release rate path that governs the change in the toughness due to the deflection process.

Inclusion of very ductile particles is becoming the most widely used method for toughening of brittle matrices. Ductile inclusions contribute to the toughness by two mechanisms, in addition to those mentioned above: bridging of the crack surfaces and the shielding of crack tip due to the straining in the process zone [3,4]. While large strong particles with high strain hardening rate provide the largest contribution to toughness by the bridging mechanism, low yield strength particles distributed in a small size tend to shield the crack more effectively [3,4]. The former mechanism is believed to be the primary source of enhanced toughness.

Ordered alloys, including intermetallics, have currently being developed for use at elevated temperatures. The Nb-Ti-Al system offers many intermetallics that can be potentially used for high temperature applications. Recently, we have been studying the phase stability and mechanical properties of $\sigma+x$ microstructures in this system [5-8]. The σ -phases occur in many systems [9] and they are undesirable phases in commercial alloys owing to their room temperature brittleness. The σ phase in the Nb-Ti-Al system has a high melting point and a high temperature strength, which make it attractive for high temperature applications [7]. The aim of this study has been to evaluate the effectiveness of dispersion of various second-phase particles in toughening the σ phase. By varying the composition and the heat treatment of alloys different inclusions have been produced. This paper reports the results of fracture

toughness measurements and fractographic analyses, and an evaluation of the toughening mechanisms in $\sigma+x$ microstructures.

Materials and Experimental Procedures

Materials

The composition of the two Nb-Ti-Al alloys investigated in this study are given in Table 1. The alloys were arc melted in the form of 200 gram buttons. Cross-sectional microprobe analysis showed no significant macrosegregation in these buttons [7].

Heat Treatment

The heat treatment schedules for the alloys studied are given in Figure 1. The as-cast microstructure of the alloys were found to be complicated, inhomogeneous, and associated with microsegregation [7]. The alloys were solutionized at temperatures above their β -transus in a purified argon atmosphere, and then cooled fast from the homogenizing temperature, which resulted in partial retention of the β -phase and the formation of metastable phases. Equilibrium microstructures were achieved by aging these alloys in the temperature range of 1000 °C to 1300 °C. The chemical analysis of the alloys after heat treatment revealed that no significant change in the alloying and interstitial contents had occurred due to solutionizing and aging processes [7].

Fracture Toughness Evaluation

Polished specimens were indented with a standard diamond Vickers indenter using a load of 10 Kgf (98.1 N) with a loading time of 15 seconds. The crack lengths produced by the indentation process were measured and used to estimate the fracture toughness values. In each sample a total of ten

indentations were applied. The fracture toughness values were calculated using three methods: (a) assuming median crack formation [9], (b) assuming Palmqvist crack formation [10], and (c) the curve fitting method suggested by Lankford [11].

In order to verify the validity of microhardness indentation as a method for measuring toughness, for comparison, selected microstructures were tested using Chevron-notched specimens [12]. Four point bend tests were performed at room temperature on a servo-hydraulic test system at a displacement rate of 4×10^{-4} mm/sec. Chevron notches were produced using a low speed diamond saw. The details of specimen geometry and data analysis are given elsewhere [13].

Microstructural Analysis and Fractography

The microstructure of the alloys were studied using electron microscopy techniques. Scanning electron microscopy was performed at an acceleration voltage of 15 to 25 KeV. Since Nb, Ti, and Al are partitioned in various phases, due to the much larger atomic mass of Nb, the microstructure could be resolved using the backscatter detector. The composition of the individual phases were determined using electron probe microanalyser. Samples for transmission electron microscopy were prepared by electropolishing using a solution of 93% methanol, 5% sulfuric acid, and 2% hydrofluoric acid at approximately -40 °C. Thin foils were examined in a transmission electron microscope operating at an accelerating voltage of 200 KeV.

An image analysis system, was used to determine the volume fraction, size, aspect ratio and the inter-particle spacing of the phases present in each specimen.

Fractographic analysis of the indented and Chevron-notched specimens were conducted using scanning electron microscopy techniques. The

backscattered imaging technique and the EDS analysis allowed the identification of various second phases on the fracture surfaces.

Results

Microstructural Analysis

The back scattered electron (BSE) micrographs of aged alloys #4 and #2 are shown in Figures 2 and 3, respectively. In both alloys the microstructure becomes coarser with increasing the aging temperature. The results of quantitative metallography are presented in Tables 2 and 3 for alloys #4 and #2, respectively. Note that in both alloys, despite the change in size and volume fraction of the particles, their length to width ratio (l/w) remained constant. The prolongation of the aging time from 16 hours to 32 hours for alloy #4 had an insignificant effect on the distribution of the phases, i.e. no further coarsening occurred upon holding.

TEM analysis has revealed [6] that the microstructure of the alloy #4 aged at 1200 °C and 1300 °C consists of the sigma (σ) phase (Nb_2Al+Ti), an intermetallic with a tetragonal crystal structure, and the beta (β) phase, a solid solution with a disordered bcc crystal structure. Upon cooling to room temperature the β phase orders to the B2 (CsCl) structure, and at slow cooling rates an orthorhombic phase (Ti_2NbAl) precipitates at the β/σ interface. The specimens heat treated at 1000 °C showed a duplex microstructure consisting of only the sigma and the orthorhombic phases [6]. The results of microprobe analysis of individual phases are given in Table 4.

The microstructure of the alloy #2 heat treated at 1000 °C and 1200 °C is composed of the sigma and the gamma phase ($TiAl+Nb$) [5,8]. At 1300 °C the β field extends toward the Al rich corner of the ternary phase diagram [14] and the microstructure of the alloy #2 consists of some β phase, which is attained upon

cooling to room temperature [15]. Table 5 presents the results of microprobe analysis of the phases for alloy #2.

Fracture Toughness

The plane strain fracture toughness, K_{IC} , of the aged alloys as evaluated by the indentation technique and using Chevron-notched specimens are given in Tables 6 and 7, and are presented in Figures 4 and 5, respectively. For alloy #4 the toughness increases continuously with the aging temperature. For alloy #2, however, the toughness increases with decreasing the aging temperature from 1200 °C to 1000 °C. Due to the absence of cracks the toughness of the 1300 °C aged specimen could not be measured by the indentation technique. Interestingly, the evaluation of the toughness using Chevron-notched specimens suggests that indeed the toughness of this specimen is not very high and we should have been able to produce cracks at the indentation load of 10 Kgf. It has been shown that the indentation technique is not a suitable method for evaluating the fracture toughness of duplex microstructures with the ductile phase as the matrix [13].

A comparison of results obtained for alloy #2 aged at 1200 °C by using Chevron-notched specimens and the indentation technique shows a reasonable correlation between the two methods. The difference in K_{IC} values calculated based on various approaches using the indentation technique is discussed elsewhere [13].

Fractography

The interaction of cracks with second phase particles was investigated in order to understand the relationship between the fracture toughness values and the microstructure of the alloys studied. This task was achieved by studying the

microcracks developed by the microhardness indentation and the fracture surface of broken notched-bend specimens. In the following each alloy is discussed separately.

Alloy #4:

Fractographic analysis of this alloy suggests that the brittle crack in sigma phase was bridged by the second phase particles, at least by the larger size particles, as shown in Figure 6a. The brittle crack penetrates partially into particles where it becomes trapped due to the ductility of the beta and the orthorhombic phases in the particle. In many cases the propagation of the crack proceeds by the reinitiation of the crack ahead of the main tip, rather than by the circumnavigation of the crack around the particle in the brittle phase. Figure 6 presents SEM micrographs demonstrating the processes of crack trapping (i.e. crack tip blunting), reinitiation of the crack ahead of the particle and in the matrix, and crack surface bridging. A crack that circumnavigates around a particle is expected to remain in the same plane, however, as Figures 6b and 6c show the crack plane changes owing perhaps to the reinitiation process. These observations suggest that the crack front is impeded by the particles to the point that the stresses ahead of the crack tip reach high enough levels sufficient for reinitiation of the brittle crack in the matrix. In general, the larger particles were found to be more effective in impeding and bridging the crack.

The interface between the sigma matrix and the particle was found to be a strong one. As can be seen in fractographs presented in Figure 7 the particles are well connected to the matrix. Consistent with the analysis of the crack profile no noticeable gross plasticity or necking of the particles was detected on the fracture surfaces.

Alloy #2:

In this alloy the interaction of cracks with particles depended on the aging treatment. For the specimen aged at 1200 °C the crack preferentially follows the σ/γ interface as is evident in the crack profile shown in Figure 8a and the protrusion of particles on the fracture surface presented in Figure 8b. For the specimen aged at 1000 °C, despite the much smaller size of the particles which is expected to make crack deflection to the interface easier, the crack followed mainly a transcrystalline path as shown in Figure 9.

The TEM micrograph presented in Figure 10 shows that the intrinsically brittle crack in the σ phase becomes blunted due to the dislocation activity and mechanical twinning in the γ phase. However, the crack profile analysis showed that for comparable sizes the β phase bridges the crack more effectively than the γ phase does, i. e. larger crack openings and longer bridged zones were observed to be associated with the β phase bridging the crack.

Consistent with alloy #4 the interface between the σ and the β phases was found to be very strong as shown in Figure 11a for the specimen aged at 1300°C. For this heat treatment, similar to the 1200 °C aged specimen, the crack follows preferentially the σ/γ interface and as shown in Figure 11b there is a large gap left between the two phases indicating the existence of tensile internal stresses in the γ particles.

Micrstructural analyses of the $\sigma+x$ alloys in the Nb-Ti-Al system [5,6] suggest that upon aging the σ phase nucleates within the grains as well as at the grain boundaries, with a specific crystallographic orientation relationship relative to the metastable β phase. Owing to the large driving force for nucleation, many nuclei form and result in a very fine σ grain size as shown in Figure 12. Despite the very fine grain size of the σ phase, as can be seen in the fractographs presented in Figures 9-11, the fracture path in this phase is very smooth. This

lack of crack deflection has been attributed to the crystallographic orientations of the σ grains [8]. As demonstrated in the TEM micrograph and the SAD pattern presented in Figure 12, in a large volume there is only a small difference in the orientation of the σ grains.

Discussion

The results of this study shows that the toughness of the σ phase in the Nb-Ti-Al system can be improved by the incorporation of the more ductile second phase particles. Figure 13 presents the toughness of the $\sigma+x$ microstructures developed in this study as a function of volume fraction of particles. As expected in a general sense the toughness is improved by an increase in the volume fraction of the less brittle phase. In the following the toughening mechanisms and the effect of aging temperature for each alloy investigated are discussed and the effectiveness of various second phases in toughening are evaluated.

A comparison between the BSE micrographs taken on polished and fractured specimens of alloy #4 indicated that the volume fraction of the particles is approximately the same as determined metallographically. The second phase particles were found to be very adherent to the σ -matrix. Therefore, it is concluded that the crack deflection mechanism does not play an important role in improving toughness in this alloy.

The fractographic observations made in this study suggest that the particles in alloy #4 contribute to toughness by crack blunting and crack bridging mechanisms. The detail of the crack bridging mechanism has been found to be different than that expected for very ductile second phase particles [4]. The initial stages of ligament behavior, i. e. small-scale yielding and the constrained

deformation of the particles apply here. However, the crack propagation does not continue by circumnavigation of the brittle crack around the particles, plastic necking and cavitation of the particles, rather by a reinitiation of the crack in the brittle matrix, as evidenced by a change in the fracture plane, and its propagation back into the second phase particle (see Figure 6). The final fracture of the ligaments, which bridge the fracture surfaces, occurs by the cleavage of the particles.

Although the particles dispersed in alloy #4 did not show gross plasticity, the increase in the toughness was considerable. An alloy of Nb-Ti-Al consisting of 100% σ phase has an average toughness of $1.9 \text{ MPa m}^{1/2}$ [7]. Incorporation of 22 volume% of particles in the 1300°C aged alloy increased the toughness to an average of $5.4 \text{ MPa m}^{1/2}$. Considering that fracture energy G and the stress intensity factor K are related by $G = K^2(1-\nu^2)/E$, where E is the Young's modulus and ν is the Poisson's ratio, and assuming $E = 100 \text{ GPa}$ [7] and $\nu = 0.3$, the increase in fracture energy is calculated to be $\Delta G = 111 \text{ J m}^{-2}$. This value is comparable to 180 J m^{-2} , which is achieved by the incorporation of ductile particles of Al in Al_2O_3 [3] for similar particle size and volume fraction.

Doubling of the volume fraction, and an order of magnitude increase in the particle size, resulted in increasing the fracture toughness from $2.0 \text{ MPa m}^{1/2}$ for 1000°C aged specimen to $3.0 \text{ MPa m}^{1/2}$ for 1200°C aged specimen, however, a slight increase (of less than 15%) in these parameters resulted in a fracture toughness of $5.4 \text{ MPa m}^{1/2}$ for 1300°C aged specimen. This pronounced improvement of the toughness can be attributed to two parameters: the nature of the particles and perhaps the size distribution of them. The particles in the 1000°C aged specimen consists of only the orthorhombic phase, however, this phase is not stable at higher temperatures and develops in alloys aged at higher temperatures only upon cooling [6]. It is suggested that the higher

toughness of the 1300 °C aged specimen is mainly due to a change of the nature of the particle to predominantly β phase, which is apparently more ductile than the orthorhombic phase. Note that the composition of the σ -phase (see Table 4) changes insignificantly with the aging temperature, and therefore, the toughness improvement is unlikely to be a result of a change in the toughness of the σ -phase. The size distribution of the particles were not measured in this study, however, as can be seen qualitatively in Figures 2 and 9, there seems to be much larger particles in the microstructure and on the fracture surface of the alloy aged at 1300 °C than at 1200 °C, despite the results of quantitative metallography (see Table 2), which reveals only a slight increase in the average particle size. A wider size distribution of particles of a given average size, i.e. existence of very large particles, may retard the crack propagation more significantly.

For alloy #2, despite an increase in the particle size and volume fraction, the toughness decreased with an increase in the aging temperature from 1000 °C to 1200 °C. Comparative analyses of the fracture surfaces of these specimens indicate that the 1000 °C aged sample shows a much less σ/γ interfacial fracture (see Figures 8 and 9). Considering that in both specimens the particles consist of only γ phase, the difference in toughness can be explained by the existence of a higher level of internal stresses in the 1200 °C specimen. As shown in Figure 11b there is a large gap between the γ phase and the σ matrix. Since the shape of the particle and the hole match perfectly and the γ phase shows limited plasticity, this gap can be attributed to the development of large elastic tensile internal stresses in the particles, which deflect the crack to the interface. These internal stresses may develop by many mechanisms; e. g. volume changes associated with phase transformation, or differences in thermal expansion coefficient. The larger size of the particles and the higher aging

temperature of the 1200 °C aged specimen are expected to result in a higher level of internal stresses. Another factor that contributes to the deflection of the crack is the higher modulus of the gamma phase (170 GPa) in comparison to the beta phase (70 GPa) [7]. The modulus of the sigma phase has been estimated to be 100 GPa, therefore on the basis of the modulus effect also one expects the crack to be attracted to the beta phase but be repelled by the gamma phase.

The increase in toughness achieved by raising the aging temperature to 1300 °C is associated with two microstructural changes; a change in the nature of the particles from γ phase to predominantly β phase, and the discontinuity of the brittle phase owing to a decrease in the volume fraction of the σ phase.

Conclusions

It has been shown that the fracture toughness of the σ phase in the Nb-Ti-Al system can be improved by a dispersion of second phase particles. In the case of beta and orthorhombic phases the particle/matrix interface is strong and the toughening is achieved by a mechanism involving crack tip trapping in the particle, crack front impediment, reinitiation of the crack ahead of the impeded crack front, crack bridging, and finally the separation of the crack surfaces by the cleavage of the particle. The γ phase is associated with a large tensile internal stresses and perhaps a low interfacial energy, and therefore, the crack is deflected and follows the σ/γ interface. The debonding process reduces the effectiveness of the particles in trapping the crack tip, and therefore, less toughening is achieved.

The toughness increased with the volume fraction of the second phase particles. Among the parameters of nature, size, interparticle spacing, and

distribution of the second phase particles, the nature of the particle, which controls the interfacial properties, the level of internal and image stresses, and the mechanical behavior of the particle, seems to be the most important one.

Acknowledgements

The authors wish to thank Pratt and Whitney for supplying the material that was used in this investigation. This research was supported by DARPA under contract numbers N00014-88-J-1100 and MD972-88-J-1006.

References

- [1] Lang, F. F., *Phil. Mag.*, Vol. 22, 1970, pp. 983-992.
- [2] Rice, R. W., *Ceramic sci. & Eng. Proc.*, Vol.2, 1981, pp. 661-701.
- [3] Sigl, L. S., Mataga, P. A., Dalgleish, B. J., McMeeking, R. M., and Evans, A. G., *Acta metall.*, Vol. 36, No. 4, 1988, pp. 945-953.
- [4] Mataga, P., *Acta metall.*, Vol. 37, No. 12, 1989, pp.3349-3359.
- [5] Hoelzer, D. T., and Ebrahimi, F., High Temperature Niobium Alloys, J. J. Stephens and I. Ahmad, Ed., TMS Publication, Pennsylvania, 1991, pp.105-119.
- [6] Hoelzer, D.T., and Ebrahimi, F., *Mater. Res. Soc. Symp. Proc.*, Vol. 194, 1990, pp. 393-398.
- [7] Castillo-Gomez, J. R., Master Thesis, University of Florida, 1990.
- [8] Ebrahimi, F., and Castillo, J. R., *Acta metall. mater.*, Vol. 40, 1992, pp.1409-1416.
- [9] Niihara, K., Morena, R., and Hassleman, D. P. H., *J. Mater. Sci. Lett.*, Vol. 1, 1982, pp.13-16.
- [10] Li, Z., Ghost, A., Kobayashi, A. S., and Bradt, R. C., *J. Am. Ceram. Soc.*, Vol. 72, No. 6, 1989, pp. 904-991.
- [11] Lankford, J., *J. Mater. Sci. Lett.*, Vol. 1, 1982, pp. 493-495.
- [12] Munz, D., Bubsey, R. T., and Shannon, Jr., J. L., *J. Am. Ceram. Soc.*, Vol. 63, 1980, pp.300-305.
- [13] Ebrahimi, F., Castillo-Gomez., J. R., to be submitted to *J. Mater. Sci. and Eng. A*, 1993.
- [14] Kattner, U. R., Boettinger, W. J., *J. Mater. Sci. and Eng A.*, Vol. 152, 1992, pp. 9-17.
- [15] Hoelzer, D. T., Unpublished results.

List of Figures

FIG. 1. Diagrams showing the heat treatment schedules for (a) alloy #4 and (b) alloy #2.

FIG. 2. BSE micrographs of polished surfaces of alloy #4 aged at (a) 1000 °C for 32 hours, (b) 1200 °C for 16 hours, and (c) 1300 °C for 32 hours.

FIG. 3. BSE micrographs of polished surfaces of alloy #2 aged for 12 hours at (a) 1000 °C, (b) 1200 °C, and (c) 1300 °C.

FIG. 4. Average K_{IC} values as a function of aging temperature for alloy #4.

FIG. 5. Average K_{IC} values as a function of aging temperature for alloy #2.

FIG. 6. BSE micrographs of crack profile in alloy #4 showing (a) crack bridging, (b) and (c) the processes of crack blunting and reinitiation.

FIG. 7. BSE fractographs of alloy #4 aged at (a) 1000 °C for 32 hours, (b) 1200 °C for 16 hours, and (c) 1300 °C for 32 hours.

FIG. 8. BSE fractographs of alloy #2 aged at 1200 °C for 12 hours showing (a) the crack profile and (b) the fracture surface.

FIG. 9. BSE fractographs of alloy #2 aged at 1000 °C for 12 hours showing (a) the crack profile and (b) the fracture surface.

FIG. 10. TEM micrograph of a $\sigma+\gamma$ microstructure showing the blunting of an intrinsically brittle crack as it enters the γ phase.

FIG. 11. (a) BSE fractograph showing the strong interface between β (grey phase) and σ (white phase) phases. (b) SEM fractograph showing debonding at the σ/γ interface. Alloy #2 aged at 1300 °C for 12 hours.

FIG. 12. (a) Bright field TEM micrograph showing many σ grains near Bragg condition. (b) Selected area diffraction pattern for the [001] zone axis of the σ phase showing the similarity in the crystallographic orientation of the grains.

FIG. 13. Fracture toughness as a function of volume fraction of particles in $\sigma+x$ microstructures.

List of Tables

Table 1. Composition of the alloys studied.

Table 2. Quantitative microscopy results. Alloy #4.

Table 3. Quantitative microscopy results. Alloy #2.

Table 4. Microprobe analysis results. Alloy #4.

Table 5. Microprobe analysis results. Alloy #2.

Table 6. Fracture toughness values for alloy #4 calculated based on (a) Palmqvist, (b) median, and (c) curve fitting models. Fracture toughness values are in MPam^{1/2}.

Table 7. Fracture toughness values for alloy #2 calculated based on (a) Palmqvist, (b) median, (c) curve fitting, and (d) using Chevron-notched specimens. Fracture toughness values are in MPam^{1/2}.

Table 1. Composition of the alloys studied.

Alloy Designation	Analysis Method	Composition (at. %)		
		Nb	Ti	Al
#2 27Nb-33Ti-40Al	Microprobe	28.2	33.7	38.1
	Wet	27.1	33.5	39.4
#4 42Nb-28Ti-30Al	Microprobe	43.0	29.0	28.0
	Wet	42.0	28.8	29.2

Table 2. Quantitative microscopy results. Alloy #4.

Heat Treatment	Phases	V_f	l (μm)	w (μm)	l/w	λ (μm)
1000°C, 16 hours	$\sigma + o$	7.7 ± 1.1	0.32 ± 0.17	0.18 ± 0.06	1.80	2.20
1000°C, 32 hours	$\sigma + o$	9.8 ± 1.6	0.36 ± 0.18	0.18 ± 0.10	2.00	1.80
1200°C, 16 hours	$\sigma + o + (\beta)$	18.0 ± 1.9	3.80 ± 1.30	2.00 ± 0.60	1.90	7.70
1300°C, 16 hours	$\sigma + \beta + (o)$	21.8 ± 2.5	4.10 ± 1.00	2.10 ± 0.70	1.95	6.30
1300°C, 32 hours	$\sigma + \beta + (o)$	23.3 ± 0.5	4.30 ± 2.00	2.30 ± 1.00	1.90	6.20

V_f = volume fraction of particles
 l = average length
 w = average width
 l/w = aspect ratio
 λ = average inter-particle spacing

Table 3. Quantitative microscopy results. Alloy #2.

Heat Treatment	Phases	V_f	l (μm)	w (μm)	l/w	λ (μm)
1000°C, 12 hours	$\sigma + \gamma$	27.9 ± 2.8	0.90 ± 0.20	0.46 ± 0.10	1.95	1.20
1200°C, 12 hours	$\sigma + \gamma$	36.6 ± 0.7	3.20 ± 1.30	1.79 ± 0.80	1.80	2.10
1300°C, 12 hours	$\sigma + \gamma + \beta$	51.7 ± 1.9	—	—	—	—

V_f = volume fraction of particles
 l = average length
 w = average width
 l/w = aspect ratio
 λ = average inter-particle spacing

Table 4. Microprobe analysis results. Alloy #4.

Heat Treatment	Phases	σ (at. %)	β^* (at. %)
1000°C, 16 hours	$\sigma + \alpha^{**}$	42.5/28.5/29.0	---
1000°C, 32 hours	$\sigma + \alpha^{**}$	42.7/28.8/28.5	---
1200°C, 16 hours	$\sigma + \beta + (\alpha)$	44.6/25.6/29.8	35.7/42.9/21.5
1300°C, 16 hours	$\sigma + \beta + (\alpha)$	44.6/25.5/29.9	35.0/42.5/22.4
1300°C, 32 hours	$\sigma + \beta + (\alpha)$	44.7/25.3/29.9	35.0/42.3/22.6

* The composition represents the β -phase at the aging temperature

** Too small to be analyzed

Table 5. Microprobe analysis results. Alloy #2.

Heat Treatment	Phases	σ (at. %)	β (at. %)	γ (at. %)
1000°C, 12 hours	$\sigma + \gamma$	34.8/29.6/35.6	—	*
1200°C, 12 hours	$\sigma + \gamma$	34.7/30.2/35.1	—	16.3/38.2/45.5
1300°C, 12 hours	$\sigma + \gamma + \beta$	37.0/26.6/36.3	23.8/39.8/36.6	19.3/34.4/46.3
1300°C, 12 hours + 1200°C, 14 hours	$\sigma + \gamma$	36.6/28.3/35.2	—	16.3/38.4/45.3

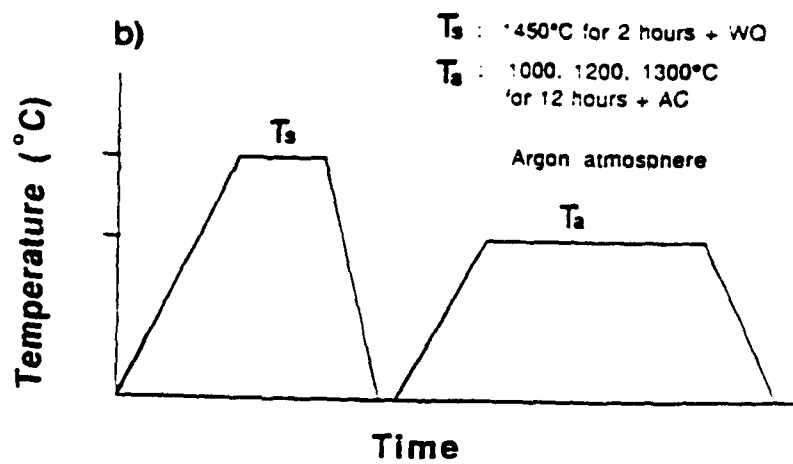
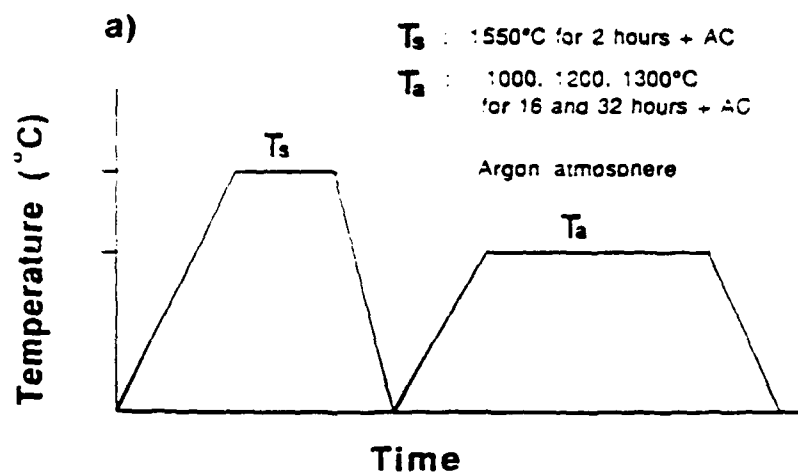
* Too small to be analyzed

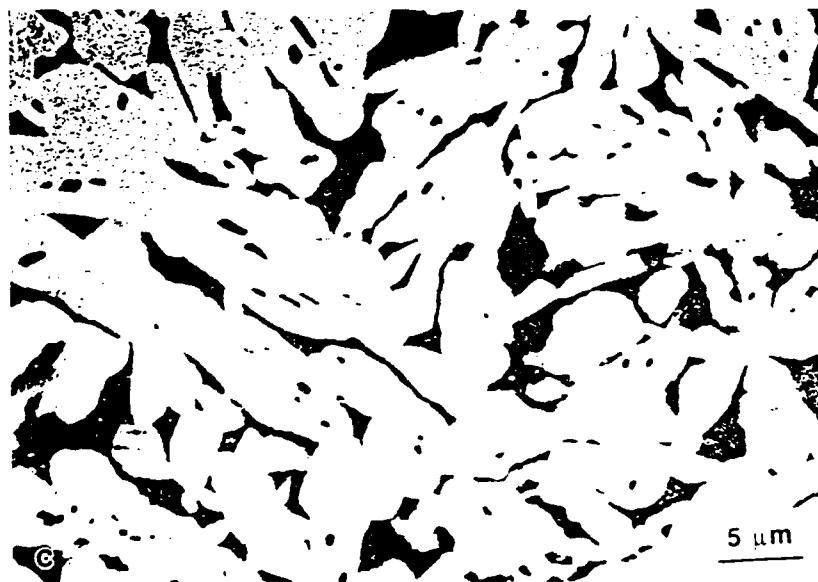
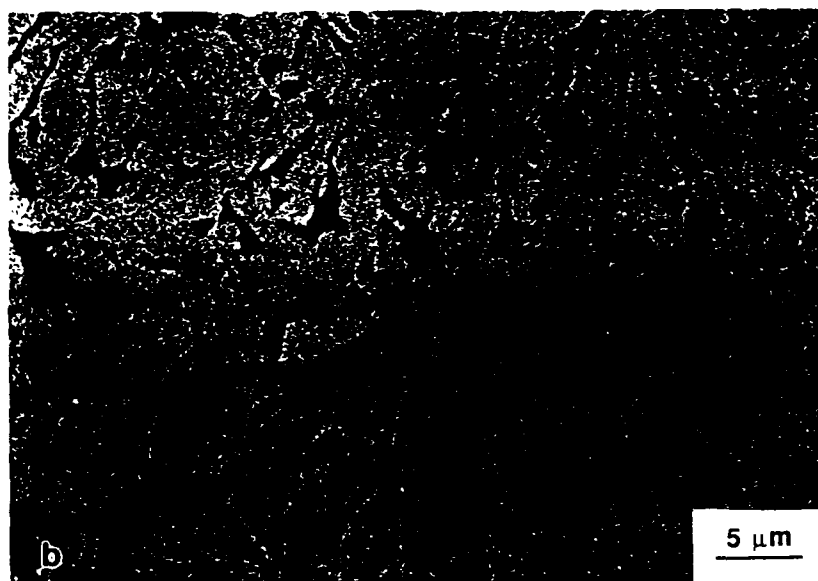
Table 6. Fracture toughness values for alloy #4 calculated based on (a) Palmqvist, (b) median, and (c) curve fitting models. Fracture toughness values are in MPa m^{1/2}.

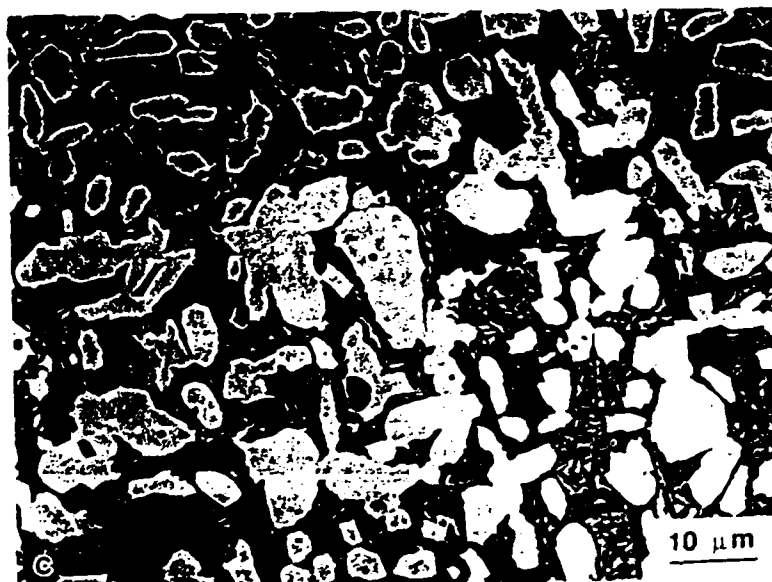
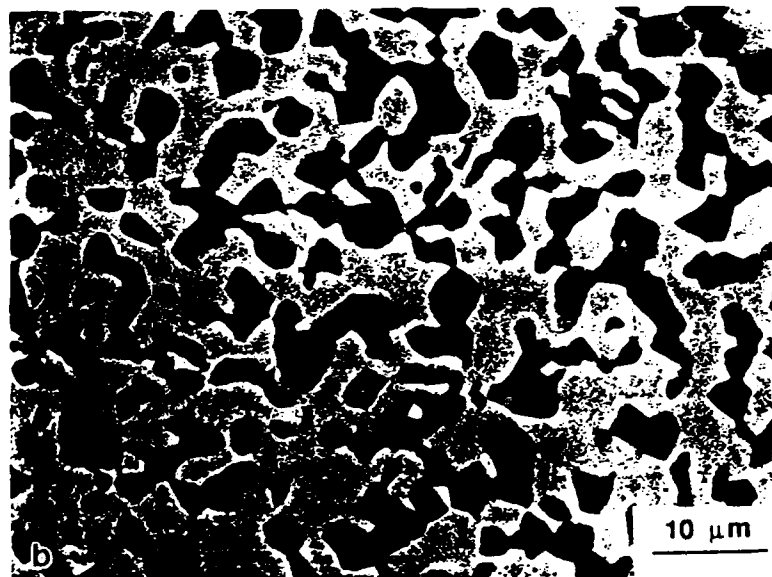
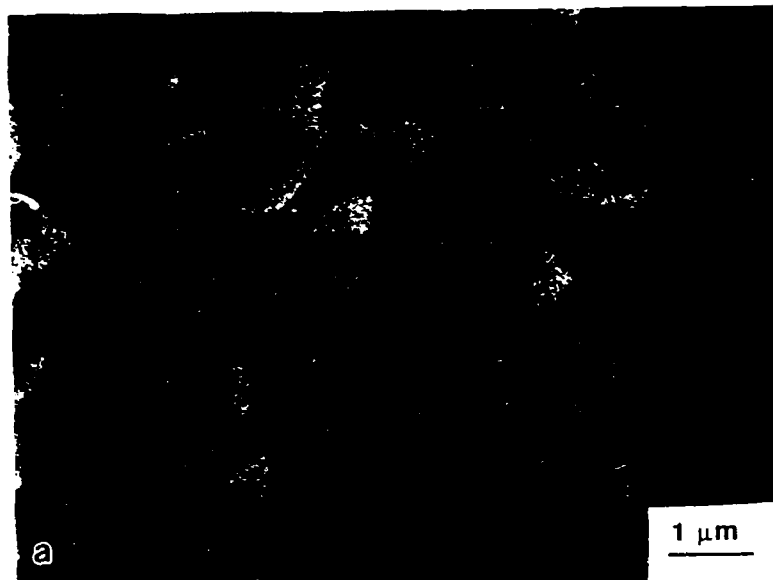
Heat Treatment	Palmqvist ^(a)	median ^(b)	Palmqvist-median ^(c)
1000°C, 16 hours	2.0 ± 0.10	2.0 ± 0.20	2.1 ± 0.20
1000°C, 32 hours	2.1 ± 0.10	2.2 ± 0.10	2.3 ± 0.10
1200°C, 16 hours	2.6 ± 0.10	3.2 ± 0.30	3.4 ± 0.30
1300°C, 16 hours	4.1 ± 0.50	5.8 ± 0.80	6.2 ± 0.90
1300°C, 32 hours	3.8 ± 0.20	5.4 ± 0.40	5.7 ± 0.20

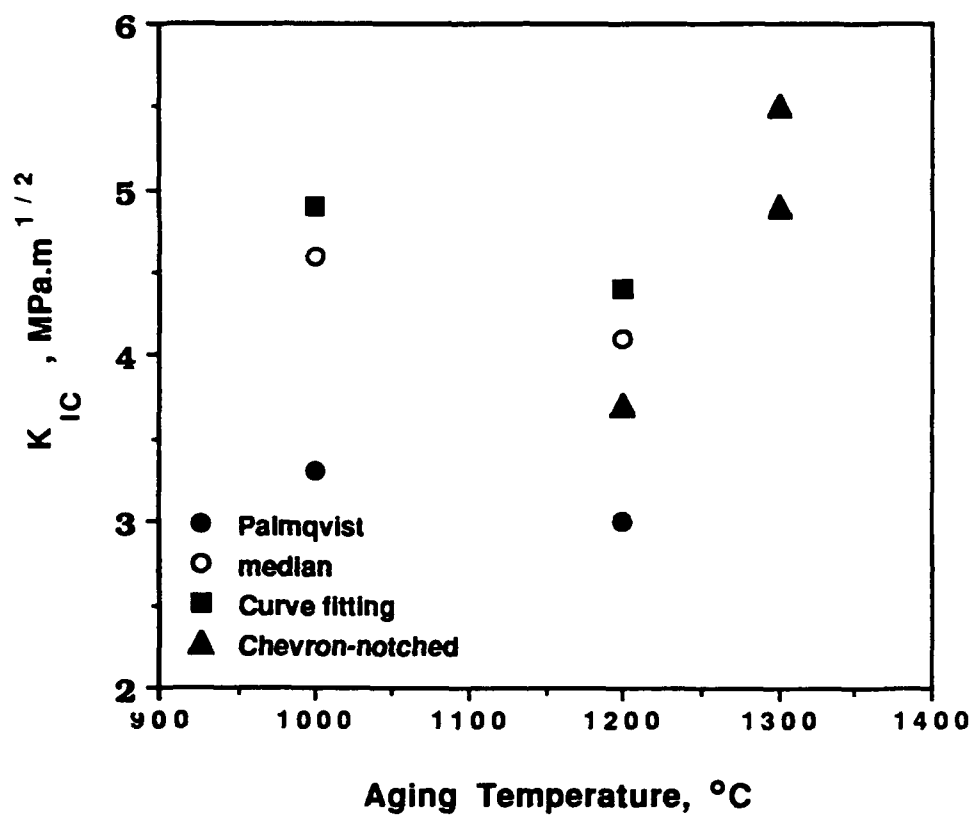
Table 7. Fracture toughness values for alloy #2 calculated based on (a) Palmqvist, (b) median, (c) curve fitting models, and (d) using Chevron-notched specimens. Fracture toughness values are in MPa m^{1/2}.

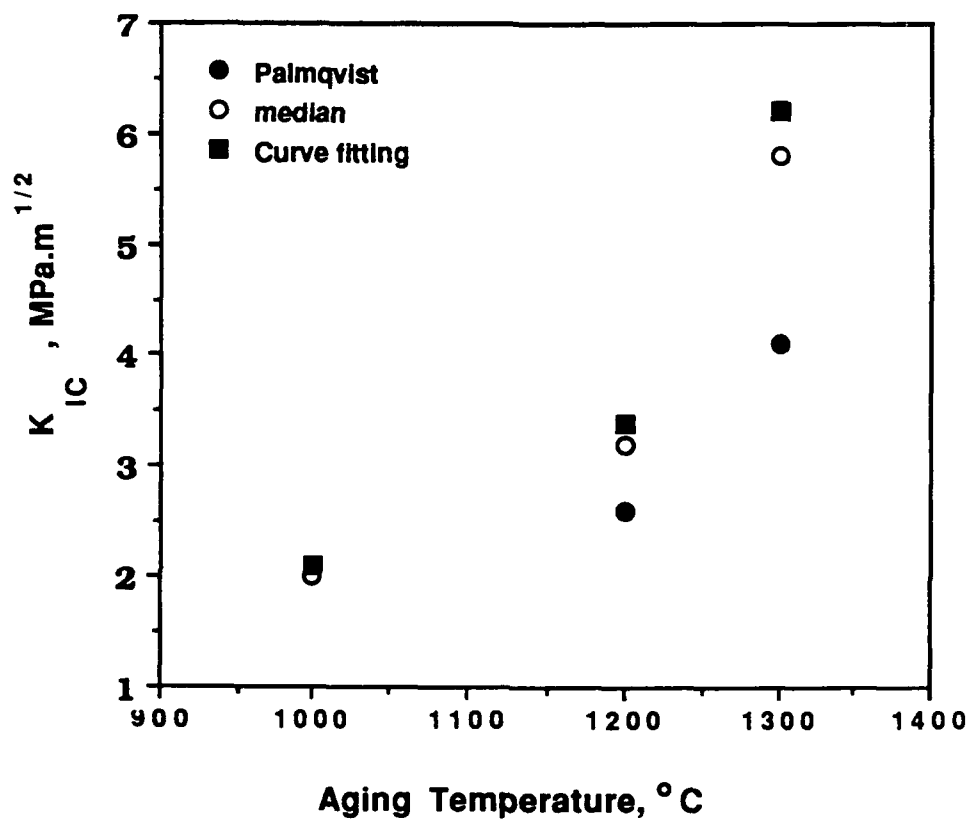
Heat Treatment	Palmqvist ^(a)	median ^(b)	Palmqvist-median ^(c)	Chevron-notched ^(d)
1000°C, 12 hours	3.3 ± 0.10	4.6 ± 0.20	4.9 ± 0.20	—
1200°C, 12 hours	3.0 ± 0.10	4.1 ± 0.10	4.4 ± 0.10	3.7 & 3.7
1300°C, 12 hours	—	—	—	4.9 & 5.5

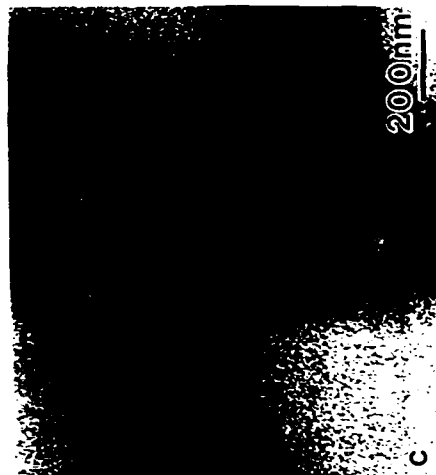




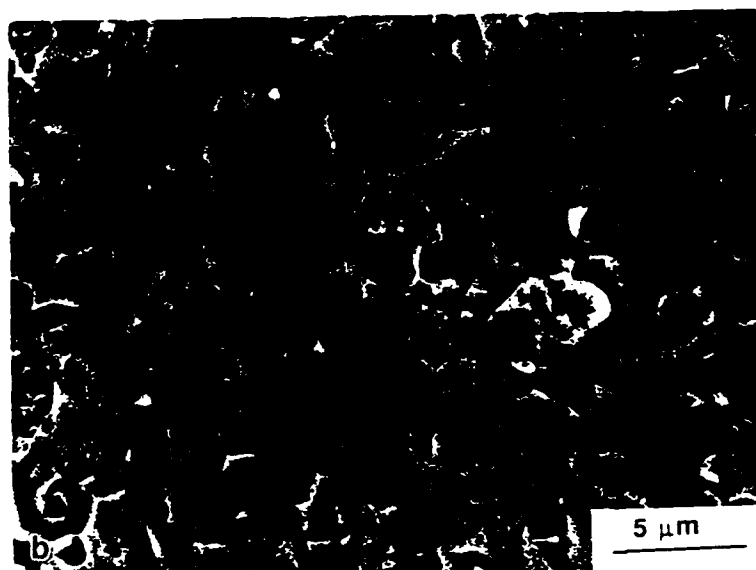


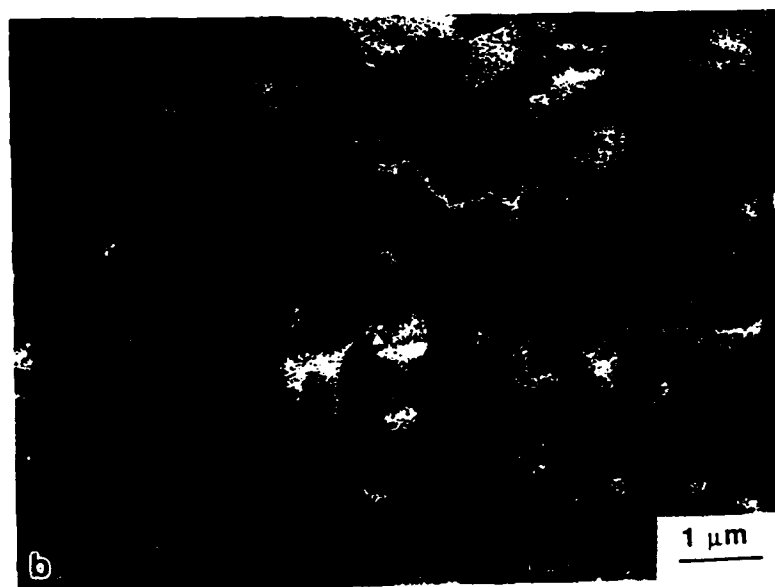
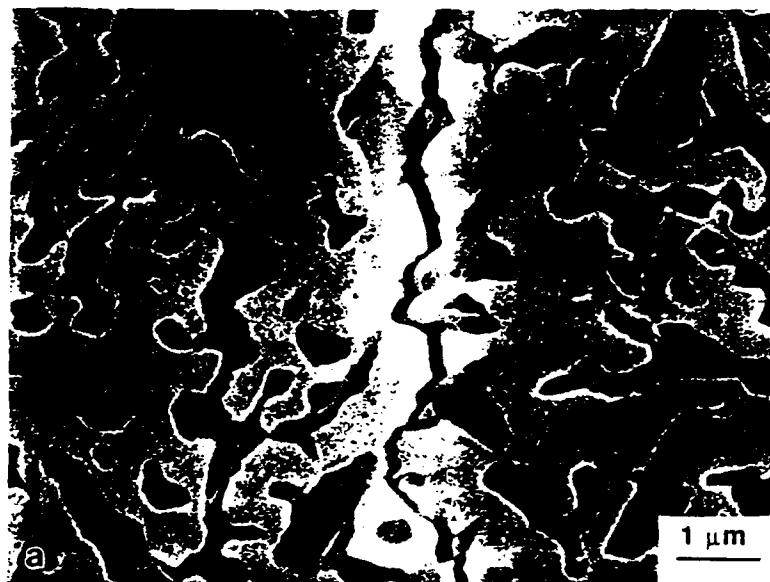


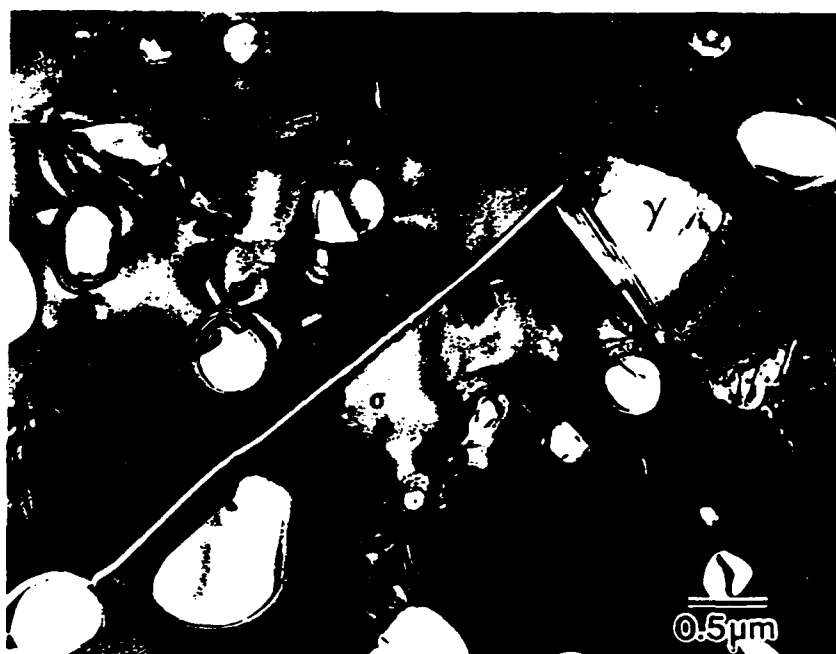


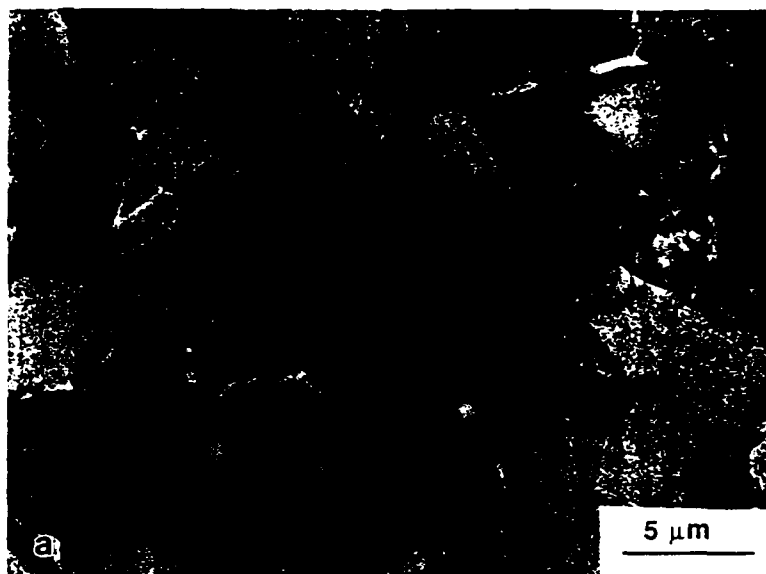


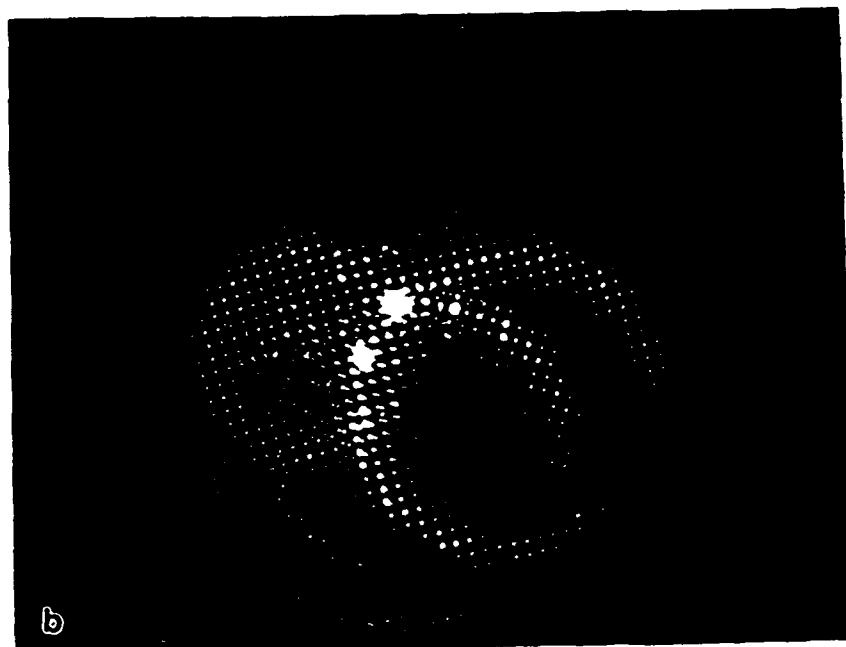












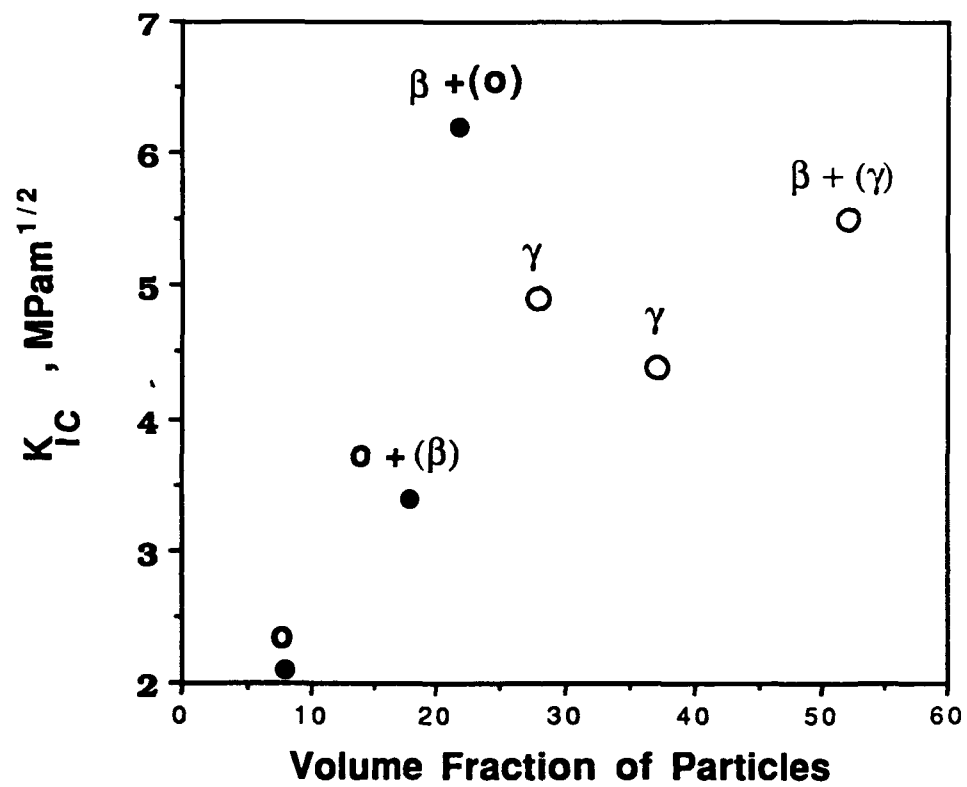


Fig. 13